The Anatomy of a Buried Submarine Hydrothermal System, Clark Volcano, Kermadec Arc, New Zealand

C.E.J. de Ronde,[1,†] S.L. Walker,[2] R.G. Ditchburn,[1] F. Caratori Tontini,[1] M.D. Hannington,[3,*]
S.G. Merle,[4] C. Timm,[1] M.R. Handler,[5] R.J. Wysoczanski,[6] V.M. Dekov,[7] G.D. Kamenov,[8]
E.T. Baker,[2,**] R.W. Embley,[9] J.E. Lupton,[9] and P. Stoffers[10]

[1] *GNS Science, 1 Fairway Drive, Avalon, PO Box 30-368, Lower Hutt 6315, New Zealand*

[2] *Pacific Marine Environmental Laboratory, National Oceanic and Atmospheric Administration, 7600 Sand Point Way NE,
Seattle, Washington 98115-6349*

[3] *Department of Earth Sciences, Marion Hall, 140 Louis Pasteur, Ottawa, Ontario, Canada K1N 6N5*

[4] *Cooperative Institute for Marine Resources Studies, Oregon State University, 2115 S.E. OSU Drive, Newport, Oregon 97365-5258*

[5] *School of Geography, Environment and Earth Sciences, Victoria University of Wellington, Wellington 6012, New Zealand*

[6] *National Institute of Water and Atmospheric Research, PO Box 14-901, Wellington, New Zealand*

[7] *IFREMER, Centre de Brest, Department of Marine Geosciences, 29280 Plouzané, France*

[8] *Department of Geological Sciences, University of Florida, 241 Williamson Hall, Gainesville, Florida 32611*

[9] *Pacific Marine Environmental Laboratory, National Oceanic and Atmospheric Administration, 2115 S.E. OSU Drive,
Newport, Oregon 97365-5258*

[10] *Institute of Geosciences, Christian-Albrechts University of Kiel, Olshausenstrasse 40, 24118 Kiel, Germany*

Abstract

Clark volcano of the Kermadec arc, northeast of New Zealand, is a large stratovolcano comprised of two coalescing volcanic cones; an apparently younger, more coherent, twin-peaked edifice to the northwest and a relatively older, more degraded and tectonized cone to the southeast. High-resolution water column surveys show an active hydrothermal system at the summit of the NW cone largely along a ridge spur connecting the two peaks, with activity also noted at the head of scarps related to sector collapse. Clark is the only known cone volcano along the Kermadec arc to host sulfide mineralization.

Volcano-scale gravity and magnetic surveys over Clark show that it is highly magnetized, and that a strong gravity gradient exists between the two edifices. Modeling suggests that a crustal-scale fault lies between these two edifices, with thinner crust beneath the NW cone. Locations of regional earthquake epicenters show a southwest-northeast trend bisecting the two Clark cones, striking northeastward into Tangaroa volcano. Detailed mapping of magnetics above the NW cone summit shows a highly magnetized "ring structure" ~350 m below the summit that is not apparent in the bathymetry; we believe this structure represents the top of a caldera. Oblate zones of low (weak) magnetization caused by hydrothermal fluid upflow, here termed "burn holes," form a pattern in the regional magnetization resembling Swiss cheese. Presumably older burn holes occupy the inner margin of the ring structure and show no signs of hydrothermal activity, while younger burn holes are coincident with active venting on the summit.

A combination of mineralogy, geochemistry, and seafloor mapping of the NW cone shows that hydrothermal activity today is largely manifest by widespread diffuse venting, with temperatures ranging between 56° and 106°C. Numerous, small (≤30 cm high) chimneys populate the summit area, with one site host to the ~7-m-tall "Twin Towers" chimneys with maximum vent fluid temperatures of 221°C (pH 4.9), consistent with $\delta^{34}S_{anhydrite-pyrite}$ values indicating formation temperatures of ~228° to 249°C. Mineralization is dominated by pyrite-marcasite-barite-anhydrite. Radiometric dating using the $^{228}Ra/^{226}Ra$ and $^{226}Ra/Ba$ methods shows active chimneys to be <20 with most <2 years old. However, the chimneys at Clark show evidence for mixing with, and remobilizing of, barite as old as 19,000 years. This is consistent with Nd and Sr isotope compositions of Clark chimney and sulfate crust samples that indicate mixing of ~40% seawater with a vent fluid derived from low K lavas. Similarly, REE data show the hydrothermal fluids have interacted with a plagioclase-rich source rock.

A holistic approach to the study of the Clark hydrothermal system has revealed a two-stage process whereby a caldera-forming volcanic event preceded a later cone-building event. This ensured a protracted (at least 20 ka yrs) history of hydrothermal activity and associated mineral deposition. If we assume at least 200-m-high walls for the postulated (buried) caldera, then hydrothermal fluids would have exited the seafloor 20 ka years ago at least 550 m deeper than they do today, with fluid discharge temperatures potentially much hotter (~350°C). Subsequent to caldera infilling, relatively porous volcaniclastic and other units making up the cone acted as large-scale filters, enabling ascending hydrothermal fluids to boil and mix with seawater subseafloor, effectively removing the metals (including remobilized Cu) in solution before they reached the seafloor. This has implications for estimates for the metal inventory of seafloor hydrothermal systems pertaining to arc hydrothermal systems.

[†] Corresponding author: e-mail, Cornel.deRonde@gns.cri.nz
*Present address: GEOMAR Helmholtz Centre for Ocean Research, Wischhofstrasse 1-3, 24148 Kiel, Germany.
**Present address: Joint Institute for the Study of the Atmosphere & Ocean—PMEL, University of Washington, 7600 Sand Point Way NE, Seattle, Washington 98115-6349.

Introduction

CLARK VOLCANO is part of the Kermadec intraoceanic arc and is the southernmost along this chain that is underlain by oceanic lithosphere not affected by continental rocks of New Zealand. The subducting slab beneath Clark and the other volcanoes of the southern Kermadec arc, however, differs from that beneath the mid and northern parts of the arc as it comprises crust of the Hikurangi Plateau, an anomalously thick sequence of Cretaceous basalt basement and sedimentary basin fill (e.g., de Ronde et al., 2007; Fig. 1).

Of the known occurrences of sulfide mineralization along the Kermadec arc, Clark is the only example where the host edifice is a volcanic cone. The others, namely Rumble II West (de Ronde et al., 2003; de Ronde, 2006; Leybourne et al., 2012a), Brothers (de Ronde et al., 2005, 2011; Berkenbosch et al., 2012; Embley et al., 2012) and Monowai (Leybourne
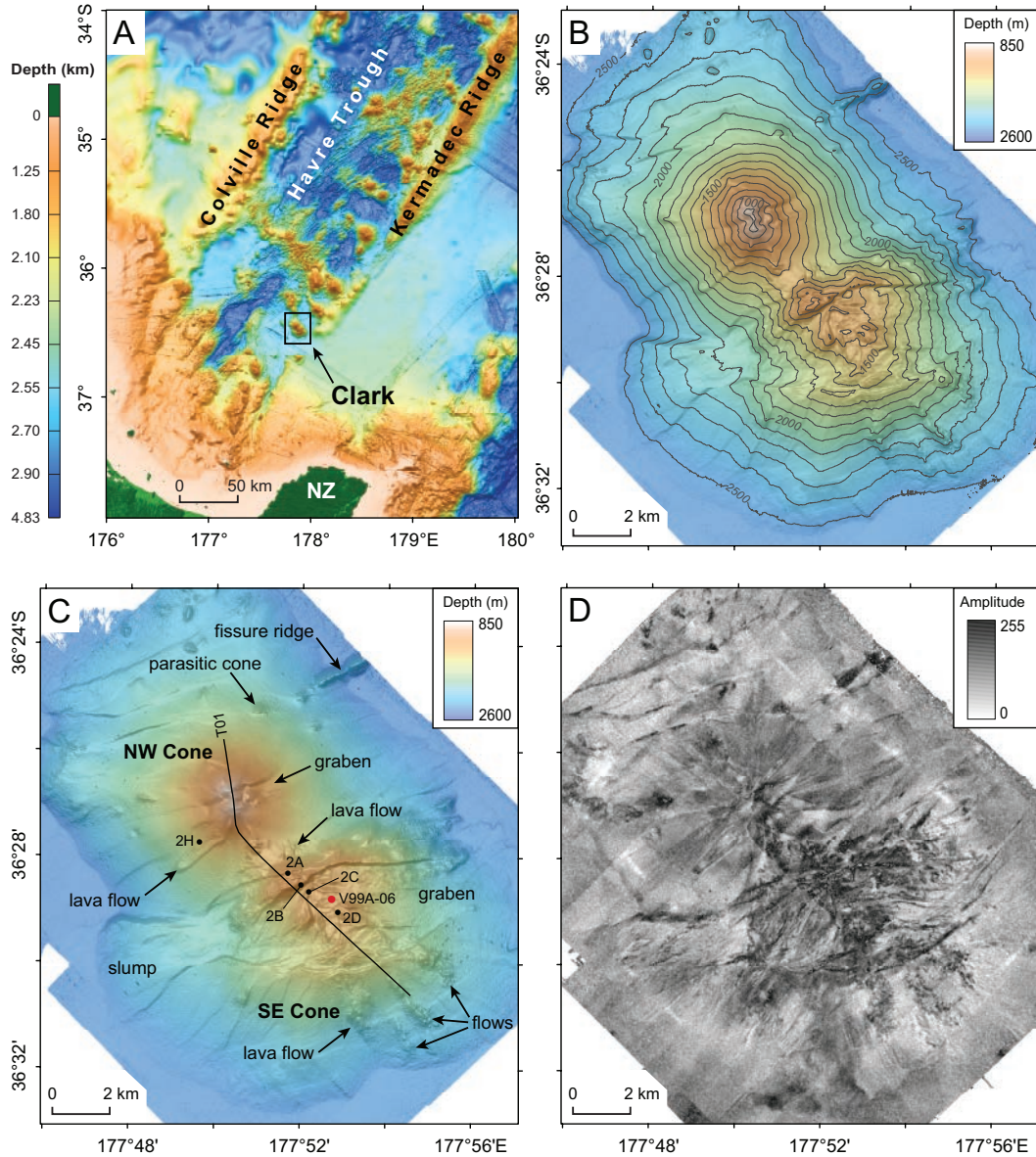

FIG. 1. A. Tectonic features of the Kermadec Ridge-Havre Trough-Colville Ridge system, northeast of New Zealand. The internal tectonic fabric of the Havre Trough backarc is regionally oblique to the trend of the two ridges, with an extension direction of ~135° near Clark volcano. The volcanoes of the active arc front (Kermadec arc) occur in the backarc just west of the Kermadec Ridge. Transverse mercator projection (CM178° E). B. EM302 multibeam data using a 15-m grid cell size to construct the bathymetric map. UTM zone 60 south projection. C. Hill shaded map of Clark volcano and its environs, which also shows the location of the 2011 NZASMS long axis tow-yo over both cones (T01), and the 1999 NZAPLUME I vertical CTDO station V99A-06 (red dot), on the SE cone (see Fig. 6D). The black dots labeled "2A" and so on relate to locations of the photographs shown in Figure 2. D. EM122 backscatter data using a 20-m grid cell size. UTM zone 60 south projection. The backscatter mosaic was created using mean amplitude values gridded in QPS Fledermaus FMGeocoder. Data for the bathymetric and backscatter maps were acquired during the 2011 NZASMS cruise. The grids were created using MBSystem software and then brought into ArcGIS whereupon the maps were constructed. Profiles of features mentioned in the text were created using QPS Fledermaus and Esri ArcGIS. NZ, New Zealand.

et al., 2012b) are all relatively deep (>1,000 m) caldera volcanoes. Caldera volcanoes of the Kermadec arc have more focused permeability, with hydrothermal fluids typically rising to the seafloor by way of ring faults. This ensures that hotter fluids (up to ~300°C) approach the seafloor before mixing with seawater. By contrast, many of the cone volcanoes along the Kermadec arc have relatively shallow summits (~100–900 m) with their geology commonly dominated by blocky lavas, pumice, ash, and volcaniclastics. This results in more widespread (and therefore less focused) permeability, with fluids expelled on the seafloor at lower temperatures (i.e., ≤220°C).

This paper focuses on the geologic and structural setting, geophysical signature, seafloor hydrothermal manifestations, hydrothermal fluid discharge, and geochemical fingerprints of Clark volcano sulfide mineralization, with the aim of characterizing "cone-type" submarine hydrothermal systems of the Kermadec arc.

Geology and Structure of Clark Volcano

Clark volcano is one of six cone volcanoes (e.g., Whakatane, Clark, Tangaroa, Rumble V, Lillie, and Rumble III) that dominate the active arc front along the southern part of the Kermadec arc (Fig. 1A). It is situated ~33 km west of the southernmost extension of the Kermadec Ridge, and ~43 km east of the Ngatoro rifts, the latter marking the deepest part of the Havre Trough at ~3,300 m. Regional fabrics are most pronounced in an area ~30 km north of Clark volcano, where numerous fissure ridges (or eruptive fissures, which are the surface expressions of dikes) 2.4 to 18 km in length (avg 7.8 km) strike ~060° (ranging 49°–73°; Fig. 1A), similar to elsewhere in the southern part of the Havre trough (Campbell et al., 2007; Casanova, 2012).

Today, Clark is a large stratovolcano comprised of two coalescing volcanic cones; an apparently younger, more coherent, twin-peaked edifice to the northwest and a relatively older, more degraded and tectonized cone to the southeast (see Fig. 1B, C). The volcano was remapped in February 2011 using an EM302 multibeam system aboard the R/V *Tangaroa*, which is also capable of producing backscatter images (Fig. 1D). The base of each edifice is defined by the 2,500-m bathymetric contour (which marks the inflection point of the volcano flanks with the surrounding seafloor); the two cones are themselves enclosed by the 1,400-m contour (Fig. 1B). The SE cone has a volume of 44.3 km³ above the 2,500-m contour to its summit at 1,157 m. It is bisected by two dominant, inward-facing, arcuate faults near the northern and southern margins of the cone that are separated by up to 3.8 km, and which have throws of up to ~200 and ~50 m, respectively (Fig. 1C). Together, the surface traces of these ~9.5-km-long faults form a southward-dipping "eye-shaped" graben structure in the center of the cone. A series of southward-dipping, highly curvilinear, sinuous- to sigmoidal-shaped normal faults occur within the graben. A large debris slide, or slump, occurs off the western flank of the SE cone that is most likely related to graben formation; it rises ~125 m off the seafloor and is up to 4 km wide near the toe of the slide (Fig. 1C). Two distinct fields of lumpy, pillow and/or lobate flows ~10 m high and ~100 m wide occur on the northern flank of the SE cone and in the saddle between the two cones. Similar flows inferred from bathymetry are oriented ~140° on the deeper, southeastern

flank of the cone and appear to be truncated by the graben structure. They stand up to ~150 m above the seafloor with widths of ~1 km and traceable lengths of ~2.5 km (Fig. 1C).

Backscatter derived from the EM302 multibeam system can be used to characterize seafloor substrates, and when combined with seafloor photography, provides documentation of the interaction between tectonic and magmatic processes. The arcuate faults marking the graben structure are clearly seen in Figure 1D, as are internal fabrics within the graben. Higher reflectivity associated with the graben demarcates exposed rock surfaces, probably as a result of the large landslide west of the edifice. Lavas on the seafloor are clearly seen on the north flank of the volcano (Fig. 2A) and mark the very steep slope of the north graben fault (Fig. 2B). Similarly, upfaulted blocks of lava occur inside the graben, with evidence at the base of one of these blocks for deposition of low-temperature Fe oxyhydroxides (Fig. 2C) and possible weak hydrothermal venting (Fig. 2D). The two fields of lobate lava flows noted above also coincide with high backscatter, as do the fissure-associated ridges on the southeastern flank of the cone (Fig. 1D).

The NW cone has a highly symmetrical profile compared to many southern Kermadec arc volcanoes (Casanova, 2012) and has a volume of 45.7 km³ above the 2,500-m bathymetric contour, rising to two separate summit peaks, both of which shoal to 851 m. A small pit crater occupies the top of the northernmost peak. These two peaks are cut by two inward-facing normal faults (e.g., Fig. 2E) separated by ~750 m, with the northern fault having a throw of ~55 m and the southern fault ~21 m. The faults trend 062° and again form a graben through the center of the cone, with evidence for sector collapse on both the western and eastern flanks of the volcano (Figs. 1C, and 4A later). A small parasite cone formed immediately east of the saddle between the two peaks and rises ~66 m above the slope, with others occurring on the lower, northeastern flank. QPS Fledermaus® software was used to determine the volume of this cone by surface differencing the EM302 bathymetric data and a vertical plane inserted at –1,160 m, constrained by a polygon with the base of the volume object the slope of the volcano flank. This small cone has a minimum volume of ~0.127 km³ above the volcano slope and is host to a shallow (~5-m deep) pit crater. Photography of the seafloor using *TowCam* shows that massive lavas crop out on the slope of the major scarp to the pit crater floor (Fig. 2F). The ridge or spur that forms the saddle between the two summit peaks (Figs. 1C, and 4A later) and others that demarcate the head scarps of slides are composed of massive lava flows (Fig. 2G). A ~500-m-wide and at least 2-km-long lava flow can be seen in the bathymetry of the southwest quadrant of the NW cone, rising ~38 m above the seafloor (Fig. 2H). Regional fissure ridges also occur in the vicinity of the NW cone, such as the one trending 060° on the distal reaches of the northeast flank. This particular ridge rises ~160 m above the seafloor with a width of ~900 m and traceable length of ~4.6 km and appears to predate cone formation (Fig. 1C). Magmatic structures such as this and the parasite cones are commonly associated with the presence of linear features (Casanova, 2012).

Backscatter results demarcate the lava flow and fissure ridge mentioned above. A small area of high reflectivity is also
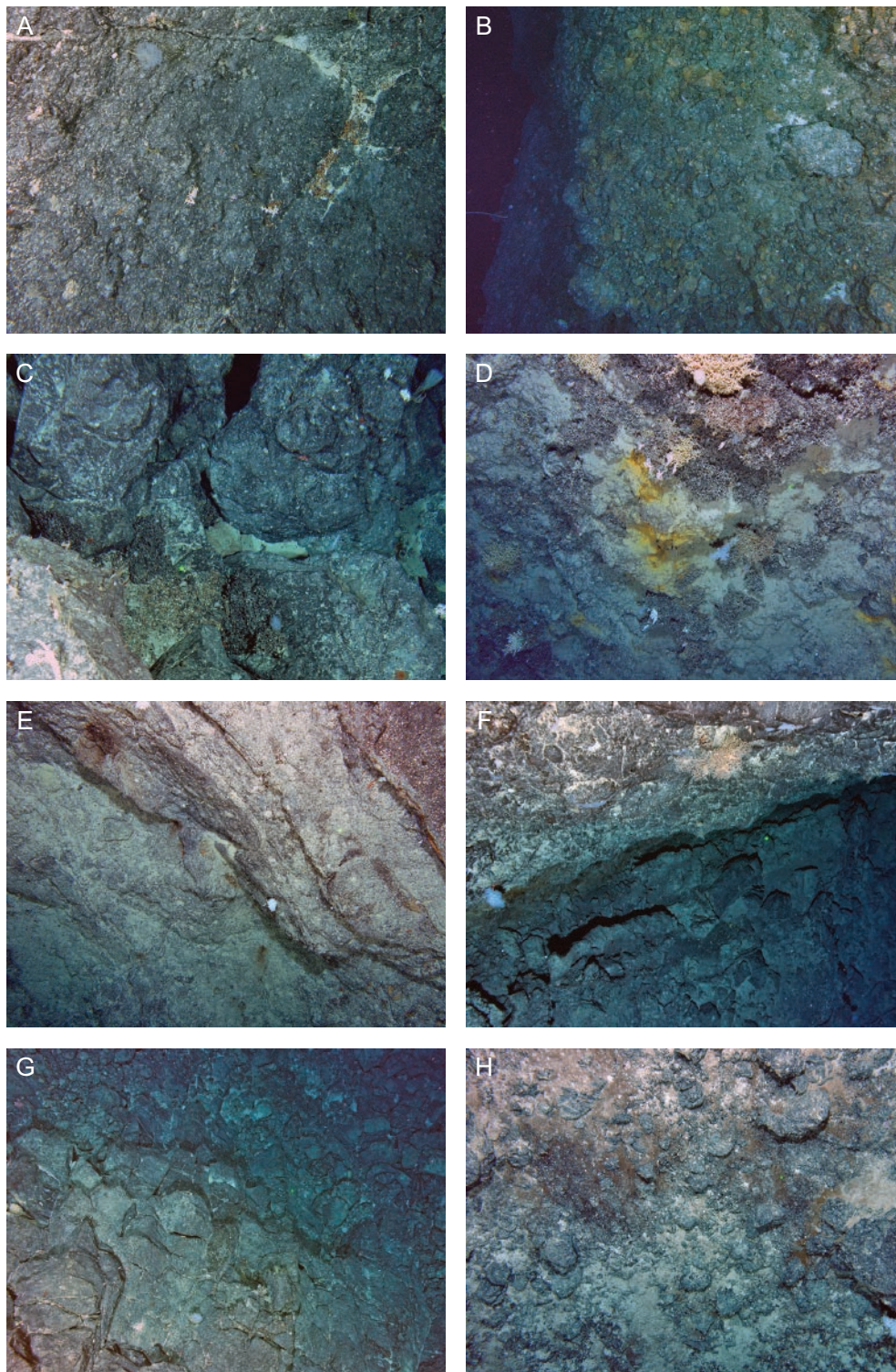
FIG. 2. Rocks of Clark volcano comprise a heterogeneous assemblage of massive to blocky lavas, pillow lavas, coarse volcaniclastic talus, localized sheet flows, and volcaniclastic sand (Wright et al. 2002; this study, see Fig. 5). A. Massive pillow lavas exposed on the northern flank of the SE cone. B. Steep escarpment on the northern flank of the SE cone graben; massive blocky lavas with lesser breccia locally. C. Exposed pillow lavas inside the graben of the SE cone, with silica between pillows. D. Blocky lava exposed at the center of the SE cone graben, where there is evidence for low-temperature hydrothermal alteration (yellow and white). E. Lavas forming the northern escarpment of the graben forming on the NW cone. F. Ridge of massive lava coming down from the summit of the NW cone, near the resurgent cone. G. More massive lava with conchoidal fractures (cf. F) near the summit of the northern peak of the NW cone. H. Blocky, poorly sorted lava flow on the southwestern flank of the NW cone. See Figures 1C and 4A for photograph locations. Standard Photoshop CS5® corrections for tone, contrast, and color were used in the images.

seen associated with the saddle ridge that separates the two smaller summit cones of the NW cone (Fig. 1D).

In this paper we focus on present-day hydrothermal activity at Clark volcano, which is concentrated near the summit of the NW cone. It is here that the submersible *Pisces V*, the autonomous underwater vehicle (AUV) *Sentry*, and towed cameras *TowCam* and *OFOS* have been mostly deployed. This is also the area where the majority of CTDO (conductivity-temperature-depth-optical) tow-yos and vertical casts were positioned. All methods used in the acquisition of geological, geophysical, and geochemical data presented in this paper are given in Appendix 1.

Volcano-Scale Geophysics

As part of our ongoing surveys of Kermadec arc hydrothermal systems, we routinely measure the gravity and magnetic anomalies associated with the volcanoes that are host to these systems. These data can be combined with seafloor bathymetry to provide insight into large, crustal-scale features pertaining to volcano emplacement and tectonism (e.g., Caratori Tontini et al., 2009, 2010). Shipboard-derived gravity and magnetic data were collected throughout the multibeam mapping of Clark volcano as part of the 2011 NZASMS (New Zealand American *Sentry* Mapping Survey) cruise.

Magnetics

The equivalent magnetization map for Clark volcano, underlain by a 15-m-resolution bathymetric grid, is plotted in Figure 3A. Almost the entire volcanic edifice is characterized by magnetization of 2 A/m, or higher, with the highest values centered either side of the saddle between the NW and SE cones in a line oriented ~west-east straddling both cones.

Gravity

Gravity anomaly data for Clark are plotted in Figure 3B and are again underlain by a 15-m-resolution bathymetric grid. There is a striking difference between the SE cone, where gravity values are as low as 244 mGal, and the NW cone where gravity values are as high as 284 mGal. The boundary between these two different regions is reasonably well delineated, has a sharp gradient, and is oriented ~053°, or subparallel to the northern boundary of the SE cone graben (Fig. 3B, cf. Fig. 1C). This boundary is not apparent in the magnetic data (Fig. 3A). Another striking feature seen in the gravity data is the nested (circular) anomaly of relatively low mGal values sitting within relatively high values of the NW cone, encompassing the upper ~350 m of the summit. Again, no apparent negative magnetization is associated with this gravity anomaly, at least at the resolution derived from sea level.

Clark Hydrothermal System

NW cone geophysics

High-resolution magnetic data were collected over the NW cone at Clark (Fig. 4) using a magnetometer aboard *Sentry*. The resulting high-resolution map shown in Figure 4C highlights a number of magnetic features associated with the NW cone summit. First, there is a ring ~1.5 km in diameter of relatively high magnetization values centered just west of the northern peak and adjoining ridge spur. Second, inside this
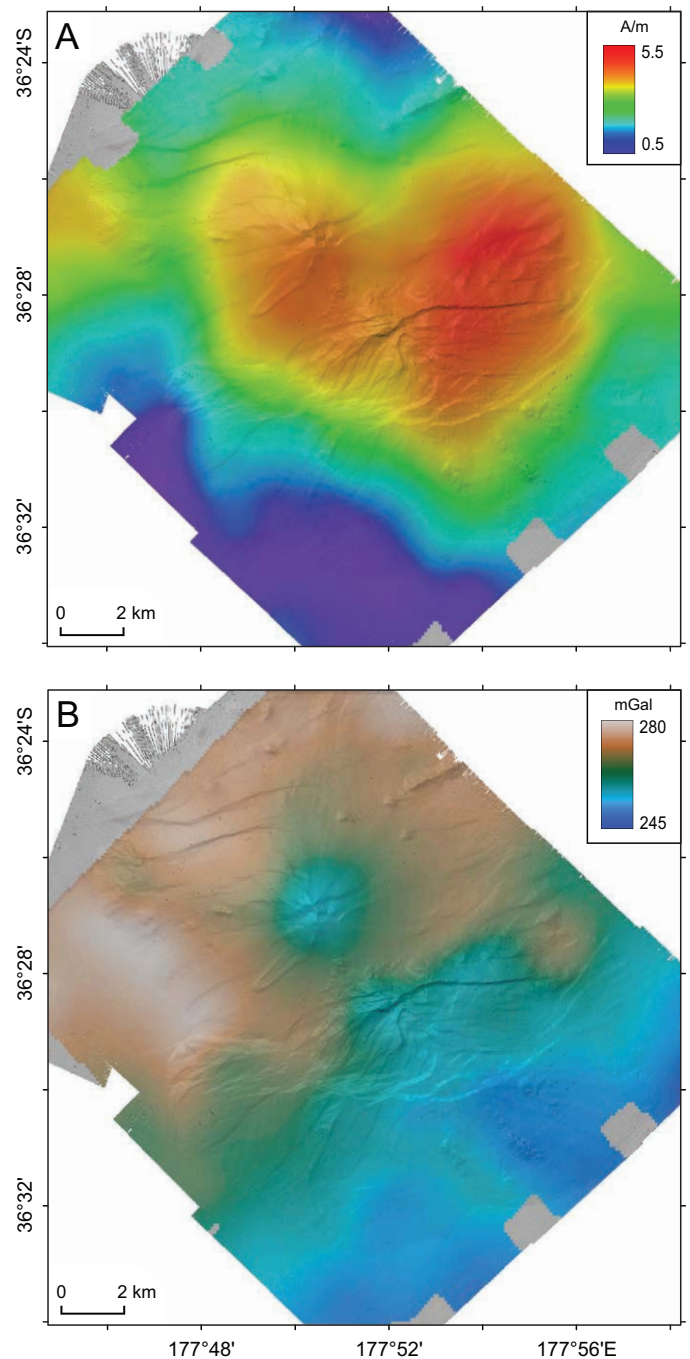

FIG. 3. A. Regional magnetic map. B. Gravity map over Clark volcano. Both edifices at Clark are highly magnetized. However, a strong gravity gradient exists between these two edifices striking in a NE direction, coincident with recent earthquake epicenters (see Fig. 14).

ring are five, predominantly oblate-shaped zones of low magnetization (dark blue, Fig. 4C). The head scarps associated with the sector collapses oriented east-northeast and west-southwest of the ridge spur (Fig. 4A) are coupled with two of these low magnetization zones. By contrast, three prominent zones of low magnetization that occur north and west of the northern peak are not associated with any flank collapse. Finally, the northern and southern boundaries of the

east-northeast collapse are marked by higher magnetization values, as are the parasite cone and spur coming down to this cone from the ridge.

Hydrothermal plumes

Three tow-yos and four vertical casts over Clark volcano (see Figs. 4-6; Table 1) show that hydrothermal activity was present atop the summit and immediate flanks of the NW cone, with δ^3He values up to 65% for water samples collected along tow T02-9A (δ^3He is the percentage deviation of the ratio in air, where δ^3He = 100 [(R/Ra)-1]). A δ^3He anomaly of 21% was also found in a sample from cast V02, immediately above the pit crater of the parasite cone on the eastern flank (Fig. 6C). Light scattering results suggest possible activity in the footwall to the northern graben fault of the SE cone, although subsequent water sample analysis for ^{3}He did not confirm this was of hydrothermal origin (Fig. 6D).

Deployment of *TowCam* during the 2011 NZASMS cruise confirmed hydrothermal activity along the ridge spur between the two summit peaks of the NW cone, as given by light scattering and temperature anomalies from an onboard CTDO system. Analysis of water samples collected in Niskin bottles attached to *TowCam* gave the highest value for δ^3He of 343% in the same general area as the chimney marked in Figure 5 (see Fig. 4A, B for location; see also Fig. 8C later). Applying a linear regression fit to 17 ^{3}He/^{4}He values, restricted to samples collected between 797 and 976 m on both sides of the aforementioned very high δ^3He sample, gave R/Ra = 7.05 ± 0.1 (R^2 = 0.99), where R = ^{3}He/^{4}He$_{sample}$ and Ra = (^{3}He/^{4}He)$_{air}$.

The AUV *Sentry* was also deployed during the 2011 NZASMS cruise with the aim of more accurately determining areas of active venting over the summit of the NW cone. Two dives (085 and 086) surveyed the two summit peaks at altitudes of 70, 40, and 20 m above bottom (mab), respectively
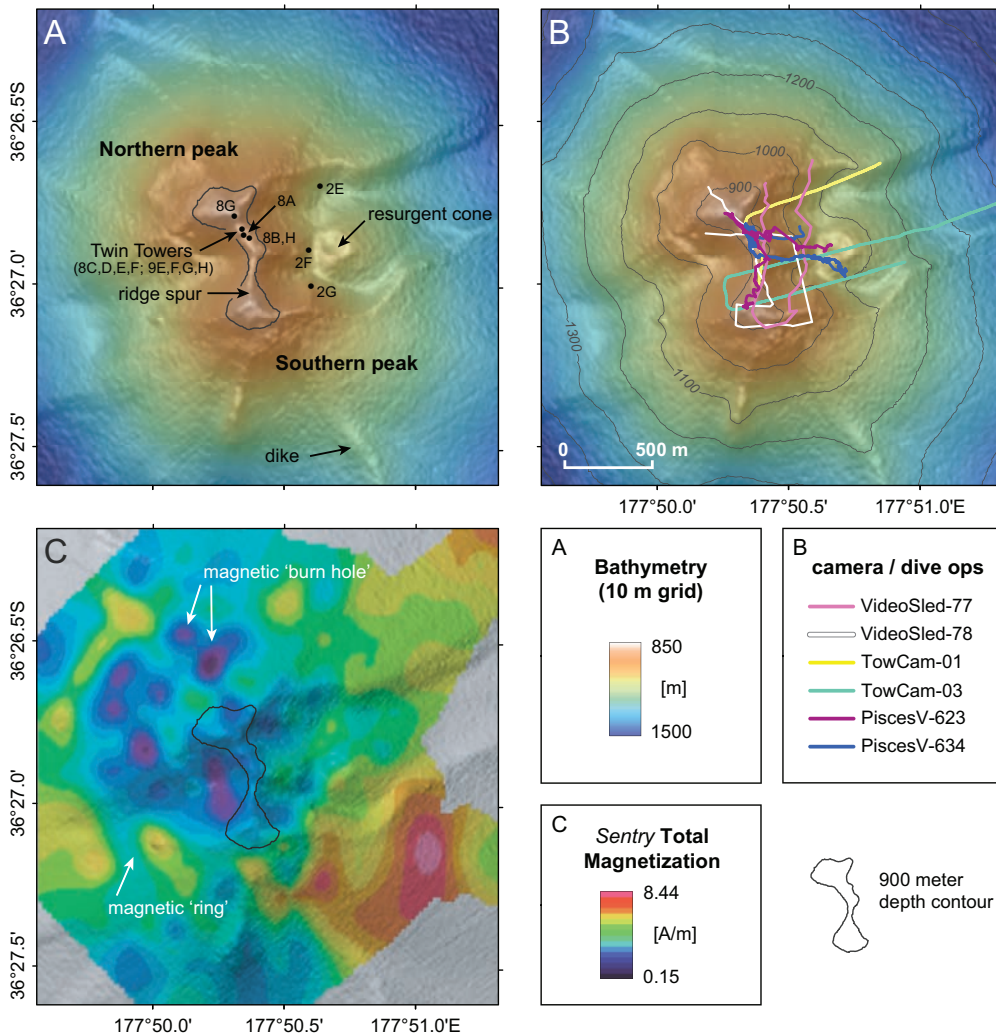

FIG. 4. A. Hill shaded bathymetric map of the NW cone summit constructed using a 10-m grid. The black dots with labels "2E," "8G," "9F" and so on relate to the locations of photographs shown in Figures 2, 8, and 9, respectively. The locations of several photographs around the Twin Towers chimney area are not resolvable at this scale. Mkr-14 was deployed during *Pisces* V dive 623 at the base of the Twin Towers chimneys, at a depth of 872 m (177° 50.3405 E, 36° 26.8282 S). B. Operations conducted over the summit of the NW cone (see Table 1). C. Magnetic anomaly map of the NW cone summit derived from data obtained by the AUV *Sentry*. A noticeable ring of high magnetization values encloses several magnetic "burn holes" (see text); the 900-m contour shown for comparison between panels.
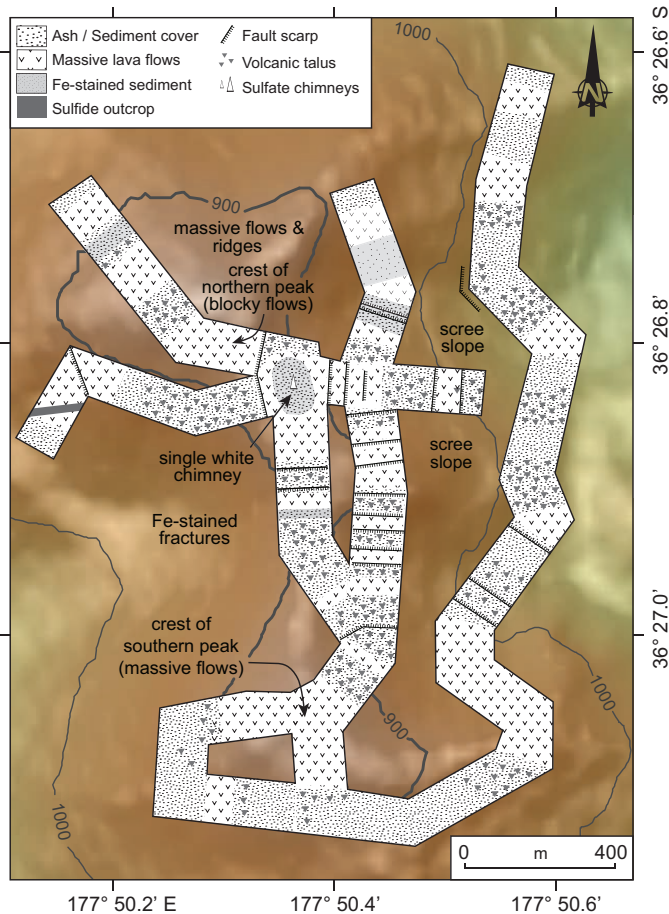
FIG. 5. *OFOS* (Ocean Floor Observation System) camera tows made using the R/V *Sonne* over the NW cone of Clark volcano. Distinct, although commonly admixed talus comprises subround autoclastic pillow talus and angular blocks typically 30 to 50 cm in diameter (Wright et al,. 2002). Elsewhere, massive lavas are common (cf. Fig. 2F, G). The *OFOS* tracks coincide with some areas along the ridge spur, in particular, visited by both *Pisces V* and *TowCam* (see Fig. 4B for track locations). The "single white chimney" located near the center of the figure is almost certainly one of the chimneys seen around the Twin Towers hydrothermal area (cf. Fig. 8C which was taken in the same area). Note that the southeastern part of *OFOS* track 78 (see Fig. 4B) is not plotted. The tracks are underlain by the EM302 bathymetry shown in Figure 4A; the 900-m contour is shown in bold for comparison with Figures 4 and 7.

(Fig. 7). The higher altitude (70 mab) survey shows elevated light scattering results over both peaks and in particular the northern end of the ridge spur. Other anomalies occur on the southwestern and northeastern flanks of the ridge, coincident with the sector collapses shown in Figure 4A and low magnetization zones of Figure 4C. A small zone of venting is located southwest of the southern peak, coincident with a small, low magnetization zone located within the circular feature of high magnetization surrounding the summit (Fig. 4C). Another slightly oblate-shaped "ring" (i.e., ~1.1–1.3 km E to W, ~1.7 km N to S) delineating low values of light scattering is centered about the ridge spur (Fig. 7A), coincident with the continuous zone of high magnetization (Fig. 4C). Oxidation-reduction potential (ORP) and dE/dt anomalies are concentrated on the east flank of the ridge spur and farther to the west, down the volcano flank. Only the ORP anomaly

on the east flank correlates with a noticeable light-scattering anomaly. The 40-mab survey only covers the eastern side of the NW cone summit, although the results are consistent with the 70-mab survey (Fig. 7B). The 20-mab survey again shows light scattering anomalies over both summit peaks, with ORP anomalies concentrated immediately west, and east, of the ridge (Fig. 7C).

Seafloor hydrothermal activity

During the *OFOS* survey of 1998, minor Fe staining was observed at the crest of the northern peak where a single, ~1-m tall, active (shimmering) barite chimney was seen on the SE side of the summit (Fig. 5). The area of staining surrounding the active chimney, observed in two separate crossings of the summit, was <90 m in diameter.

The *TowCam* surveys of 2011 only partially transected areas of hydrothermal activity, with TC-03 crossing the pit crater of the small parasite cone, and the ridge spur of the NW cone twice, whereas TC-01 more closely followed the ridge spur for ~400 m at the end of its survey (Fig. 4B). Iron staining was seen inside the pit crater of the parasitic cone (Fig. 2F), consistent with water column evidence for weak hydrothermal activity at this site. TC-01 also confirmed Fe staining near the northern peak that extended ~200 m along the ridge spur (Fig. 8A, B; see Fig. 4B for location). *TowCam* passed over the top of an active chimney at the northern end of the ridge spur, which was venting clear, shimmering fluid (Fig. 8C), similar to that seen by *OFOS* 13 years earlier.

The submersible *Pisces V* made two dives on the NW cone at Clark; PV623 and PV634 (Fig. 4B). Dive PV623 landed in the pit crater of the parasitic cone, then moved westward climbing up the head scarp of a sector collapse (Fig. 4A) before reaching the ridge spur and the previously identified area of active hydrothermal venting. Here, there was abundant, diffuse, low-temperature venting associated with Fe oxyhydroxide-silica deposits (Fig. 8D). This main vent field covers an area ~100 m in diameter and includes numerous chimneys, including the two large "Twin Towers" (Fig. 4A; see below) and almost certainly is the same area passed overtop by *TowCam* six years later. Farther upslope, near the summit of the northern peak, diffuse venting was again prevalent, emanating either from layered, hydrothermally altered volaniclastic rocks (Fig. 8E), or cracks in the upper surface of the same rocks (Fig. 8F); in both cases venting was associated with abundant long-neck barnacles *Volcanolepas osheai* (Eolepadidae). Other vent-related animals included the mussel *Giganidas gladius* (Mytilidae) and a pink scale worm (Polynoidae).

Farther to the south, dive PV623 encountered thick (10s cm) crusts of barite-rich volcaniclastic material on the ridge linking the northern and southern peaks (Fig. 8G), together with Fe oxyhydroxide-rich crusts that in places have cavities filled by spongy silica (Fig. 8G). Bacterial mats were seen locally, with flocculent bacteria being expelled from some seafloor cavities discharging fluids up to 55°C. Small, Fe oxyhydroxide chimneys have grown out of the lava substrate of green and red nontronite crusts, with greenish filamentous material nearby. Mounds ~4 to 5 m in diameter and ~1.5 m in height, covered with barnacles and interlayered with Fe oxyhydroxide layers, also occur along the ridge spur (Fig. 8H) and are thought to represent the base of old chimneys. No evidence
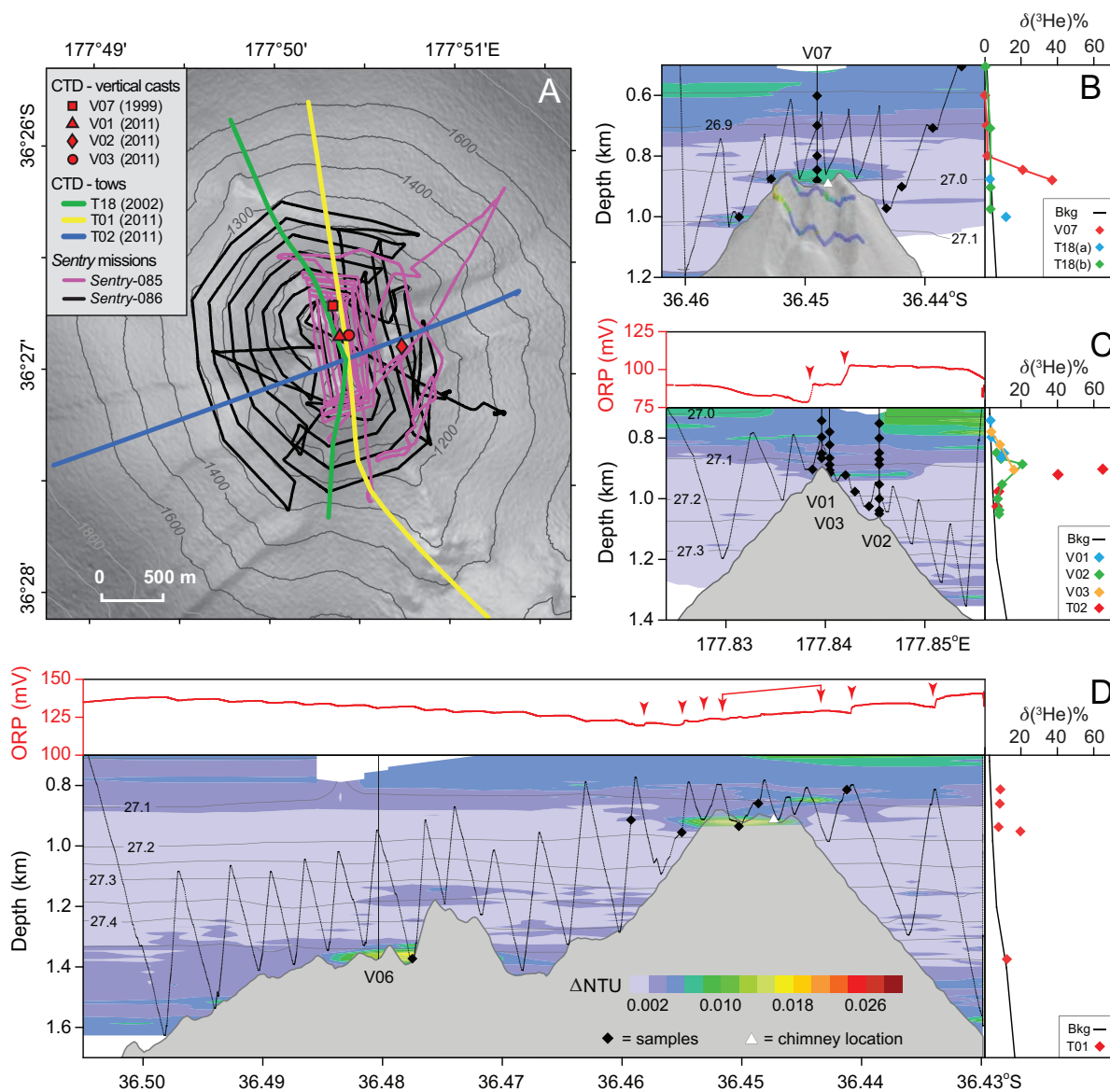
FIG. 6. Optical backscatter (ΔNTU) transects, ORP data, and δ(³He)% profiles over Clark volcano. For all ΔNTU transects (i.e., B, C, and D): the black saw-tooth line shows the oscillating path of the CTDO during tow-yo operations; ΔNTU color scale is shown in (D); vertical black lines show vertical CTDO cast positions; white triangles indicate the location of known hydrothermally active chimneys near the summit (B and D); black diamond symbols (♦) show locations of discrete water bottle samples. ORP data were available for 2011 tows only (C and D); small red arrows indicate significant hydrothermal anomalies. For all δ(³He)% profiles: the black line is the regional background profile; vertical cast symbols are connected but tow symbols are not (as tow samples are horizontally spaced and not true vertical profiles). A. NW cone at Clark showing summit bathymetry (100-m contour lines) with locations of CTDO vertical casts (red symbols), CTDO tows (yellow, blue, and green lines) and *Sentry* mission track lines (pink and black lines). B. ΔNTU transect from CTDO tow T18 (2002) plus ΔNTU values overlaid on the bathymetry along the path of video sled tow SO135-77OFOS (from a MAPR mounted on the sled; color scale is same as for contoured transects; hill-shaded bathymetry as viewed from the northeast perpendicular to path of tow T18 over the summit). δ(³He)% profiles are given for V07 (1999) and T18 (2002). Tow T18 samples are separated into two groups: samples taken south of the summit (blue symbols, not connected) were spatially separated from the samples taken during the final upcast of the tow (green symbols, connected), which approximated a vertical CTDO cast. C. ΔNTU transect and ORP data from CTDO tow T02 (2011). δ(³He)% profiles for V01 (2011), V02, (2011), V03 (2011), and T02 (2011). D. ΔNTU transect, ORP data, and δ(³He)% profile for T01 (2011). The region over the summit in (D) had a long, slow decrease in ORP (cf. a rapid drop as seen in C) but is considered significant. The magnitude of the anomalies (i.e., total change from "background" values to minimum, before the value started increasing again) in C are ~12 mV; the first three anomalies along T01 in (D), beginning at the right side of the plot, are ~6 mv each. The last three are smaller (~2–3 mv). For full station names used for the various casts, see Table 1. Abbreviations: Bkg = background, CTDO = conductivity-temperature-depth-optical. MAPR = miniature autonomous plume recorder.

TABLE 1. Cruises and Operations Related to the Clark Volcano Hydrothermal System[1]

Year	Research vessel	Cruise	Operation	Station	Location	Comment
1998	*Sonne*	SO135	OFOS	SO135-77	NW cone	Summit camera tow
			OFOS	SO135-78	NW cone	Summit camera tow
			Dredge	SO135-74	NW cone	Summit dredge with MAPR
1999	*Tangaroa*	NZAPLUME I	CTDO	V99A-06	SE cone	Summit vertical cast
			CTDO	V99A-07	NW cone	Summit vertical cast
2002	*Tangaroa*	NZAPLUME II	CTDO	T02A-18	NW cone	~N-S tow-yo
			CTDO	V02A-52	N of Clark	Vertical cast
			CTDO	V02A-53	S of Clark	Vertical cast
2005	*K-o-K*	NZASRoF	Sub	PV-623	NW cone	Dive along saddle
			Sub	PV-634	NW cone	Dive along saddle
2011	*Tangaroa*	NZASMS	AUV	*Sentry*-085	NW cone	Summit survey
			AUV	*Sentry*-086	NW cone	Summit survey
			TowCam	TC-01	NW cone	Saddle and NE fault
			TowCam	TC-02	NW cone	SE cone
			TowCam	TC-03	NW cone	Pit crater
			TowCam	TC-04	NW cone	Lava flow on SW flank
			CTDO	TAN1104-T01	both cones	~N-S and NW-SE tow-yo
			CTDO	TAN1104-T02	NW cone	WSW-ENE tow-yo
			CTDO	TAN1104-V01	NW cone	Saddle vertical cast
			CTDO	TAN1104-V02	NW cone	Pit crater vertical cast
			CTDO	TAN1104-V03	NW cone	Saddle vertical cast

Notes: AUV = autonomous underwater vehicle; CTDO = conductivity-temperature-depth-optical; *KoK* = *Ka'imikai-o-Kanaloa*; MAPR = miniature autonomous plume recorder; NZASMS = New Zealand American *Sentry* Mapping Survey; NZAPLUME = New Zealand American PLUme Mapping Expedition; NZASRoF = New Zealand American Submarine Ring of Fire; OFOS = Ocean Floor Observation System; PV = *Pisces V*; SO = *Sonne*; Sub = submersible; T = tow; TAN = *Tangaroa*; TC = *TowCam*; V = vertical; for location of the various operations, see Figures 1C, 4B, 5, and 6

[1] *TowCam* TC02 was a traverse over the northern margin of the SE cone

for hydrothermal activity was seen on the southern peak, although *Sentry* water column data suggest there may be diffuse venting on the southeastern flank of this peak (Fig. 7). *Pisces V* dive PV634 also traversed westward up the same head scarp as PV623 and similarly moved northward to sample the vents on the spur just south of the northern peak (Fig. 4B).

Mineralized samples

Dredging of the summit area in 1998 by the R/V *Sonne* sampled a thick barite crust and clay-altered basalt breccias. The largest sample recovered consisted of a 25-cm-thick block of coarse barite sand with altered volcanic fragments (Fig. 9A; cf. Fig. 8G). The barite sands contain about 75 to 80% coarse granular barite in a matrix of amorphous silica—which cements the sand and locally fills open cavities—and clay minerals. The barite was likely eroded from massive barite mounds, or chimneys. The clays are inferred to be Mg smectites, based on electron microprobe data (not shown), and are derived from the alteration of volcanic material in the sediments. All of the samples had a thin Fe-Mn oxide coating, suggesting that they are old. The absence of anhydrite in the barite sand implies that it was not recovered from an area of active venting. By contrast, the hydrothermal crusts do contain significant anhydrite and therefore were likely actively forming at the time of sampling.

In the week before the 1998 *Sonne* cruise SO-135, fishermen reported that sulfides were recovered in nets from a location near the summit of the NW cone, at a water depth of ~800 m (cf. Fig. 4A with Figs. 5–7). These samples in part looked like chimney fragments (Fig. 9B) otherwise they consisted of finely laminated crusts of pyrite, marcasite, barite, and massive anhydrite (Fig. 9C), or mineralized breccia

(Fig. 9D). They are typical of low-temperature hydrothermal precipitates at active seafloor hydrothermal vents and again probably originated from larger mounds, or chimneys. Given the reported depth and type of the fisherman's samples, they almost certainly come from chimneys seen (and sampled) by *Pisces V* on the northern peak of the NW cone.

Chimneys that discharged clear hydrothermal fluid between 56° and 106°C were observed in the main vent area described above and include delicate spires several 10s of centimeters to ~1 m in height, commonly associated with long-necked barnacles (Fig. 9E, F). All the chimneys had exteriors that were knarled and bulbous and are typically composed of anhydrite + barite + pyrite and marcasite. Several were sampled for geochemical analysis and dating.

The Twin Towers chimneys represent the most striking feature of the main vent area (Fig. 4A), comprising two separate chimneys standing side by side, reaching up to 7 m in height. Fluids venting near the top of one of the spires measured 185.2°C (Fig. 9G); hydrothermal fluid expelled near the base of these chimneys had temperatures up to 221.1°C and pH down to 4.88 (Merle et al., 2006). These chimneys are built on top of a large sulfide mound (Fig. 9H). Both the Twin Towers and other small chimneys in the area appear to be aligned perpendicular to the slope of the ridge.

We can summarize the different mineralization types seen at Clark as follows: (1) barite-rich, (2) barite-pyrite, (3) barite-anhydrite, (4) anhydrite-rich, (5) silica, (6) Fe-Mn-silica, (7) silica-clay, and (8) barite-silica-clay.

Mineralogy

Polished thin sections show a predominance of prismatic anhydrite and radial barite laths intergrown with subhedral to
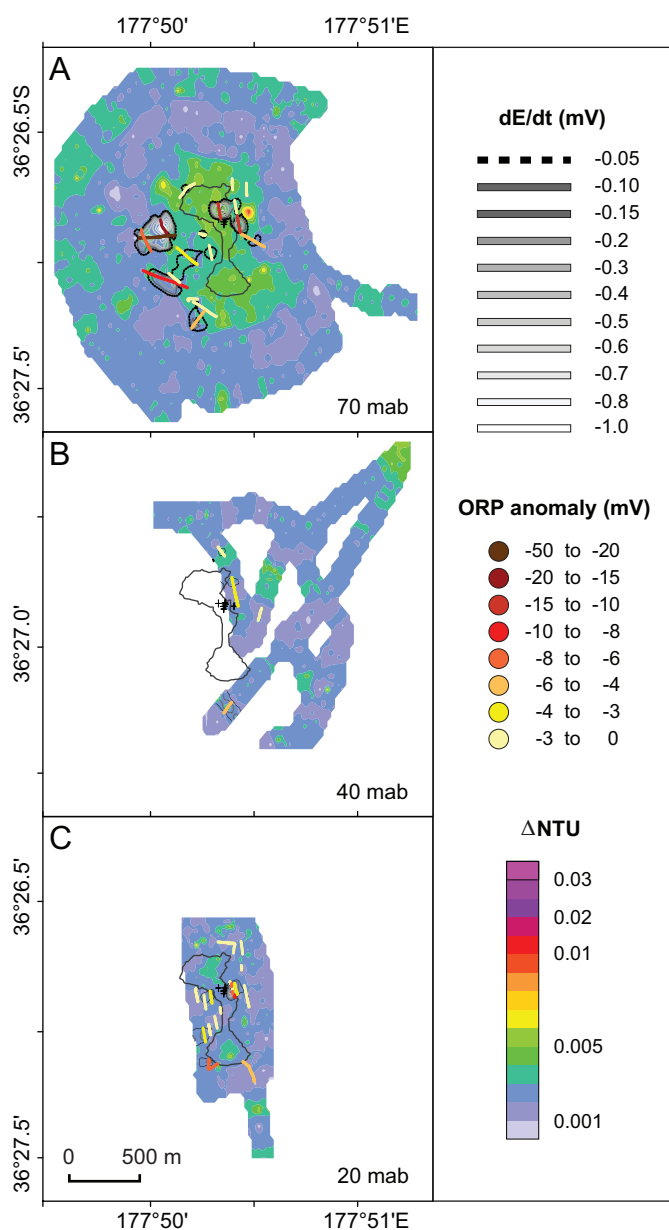
FIG. 7. *Sentry* dive 085 began its survey at 20 m above bottom (mab) for the first 8 hours, then travelled at 40 mab above bottom for the last 7.25 hrs of the dive. Dive 086 was at 70 mab for the entire dive. A. Survey 70 mab. B. Survey 40 mab. C. Survey 20 mab. *Sentry* itself houses a Seapoint optical backscatter sensor and an ORP sensor, although the data presented in this figure were all compiled from MAPR data. Using dE/dt for the *Sentry* data is more instructive than for the CTD data since some of these anomalies have very small dE/dt (i.e., were slow to change) but overall have significant decreases. Crosses shown in the maps are chimney locations taken from the observation logs for the camera tow SO135-78-OFOS and *Pisces* dive PV-623. For reference, the thin black line in the center of each figure is the 900-m bathymetric contour (cf. Fig. 4A, C).

euhedral pyrite ± marcasite (cf. Fig. 9B). A later generation of colloform pyrite mantled earlier, more euhedral pyrite in the relatively porous matrix of the crustlike examples of mineralization (cf. Fig. 9C). Minor sphalerite and galena were seen in some chimney samples. X-ray diffraction analysis of select chimney samples, including the "fisherman" chimney,

confirmed they are dominated by anhydrite with gypsum and barite, and lesser pyrite ± marcasite. Secondary electron images and energy dispersive X-ray spectra again show the samples are dominated by sulfates and pyrite. For example, blades of anhydrite that locally show evidence for dissolution (Fig. 10A) are coated by 10-μm grains of pyrite (Fig. 10B). Elsewhere, fronds of barite (Fig. 10C) are seen in the matrix to several of the chimneys, as are barite lepispheres (Fig. 10D). Barite is also seen in its typical radial, or rosette habit in these chimneys (Fig. 10E). Other samples show botryoidal pyrite intergrown with barite laths (Fig. 10F) and still others show euhedral pyrite (and barite) covered by small blebs of opal (Fig. 10G). Finally, colloform Mn oxides can be seen coating anhydrite (Fig. 10H).

Geochemistry

The composition of Clark volcano was first described by Gamble et al. (1997) who reported geochemical analyses of eight samples dredged from the NW cone (Fig. 4). Samples from this edifice ranged from basaltic to basaltic andesite, with a single dacitic sample collected northwest of the main cone. Petrographically, the basalts and basaltic andesites are distinct, with the former having a phenocryst assemblage of olivine and clinopyroxene and the latter being olivine free and containing abundant plagioclase. This is reflected in their chemistry, with the basalts having high MgO and Ni (~9 wt % and 70 ppm, respectively) compared to the basaltic andesites (~5.5 wt % and 20 ppm). Although the basaltic andesites were considered to be typical of the southern Kermadec arc, the basalts were termed K-rich (or high K) basalts due to their unusually elevated K contents (~2% K_2O at 50% SiO_2) when compared to the basaltic andesites (~0.35% K_2O at 52% SiO_2). This K-rich suite was also notable in its elevated LILE and LREE contents (Fig. 11) and more radiogenic isotopic compositions (e.g., $^{87}Sr/^{86}Sr$ >0.7051; cf. <0.7045 for all other southern Kermadec arc and Havre trough rock samples; Gamble et al., 1997; Todd et al., 2010; see below).

More recent studies similarly reported geochemical analyses of southern Kermadec arc and Havre Trough samples. These include higher precision analysis of Clark volcano samples (including those reported by Gamble et al., 1997) that confirm the high K nature of the basalts (Haase et al., 2002; Wysoczanski et al., 2012) and the highly enriched sediment component preserved in these samples (Todd et al., 2010). Comparison of the basaltic-andesite samples from Clark volcano with samples from other arc front volcanoes now show them also to be distinct in composition. Notably, they have lower K (and are termed "low K" here) and have REE, Th, U, and Na contents that are particularly depleted compared to other Kermadec arc front samples, and are more similar to backarc basin samples.

Mineralized samples

The mineralized crusts recovered from Clark typically contain subequal amounts of barite and anhydrite (~40 wt % $BaSO_4$ vs. 37 wt % $CaSO_4$), up to 7 wt % SiO_2 as amorphous silica, and 15 wt % pyrite ± marcasite. In general, the pyrite-bearing samples are notably enriched in Ag (up to 350 ppm) and Au (up to 15.1 ppm) when compared to the other samples (Appendix 2A). Arsenic contents are also significantly higher
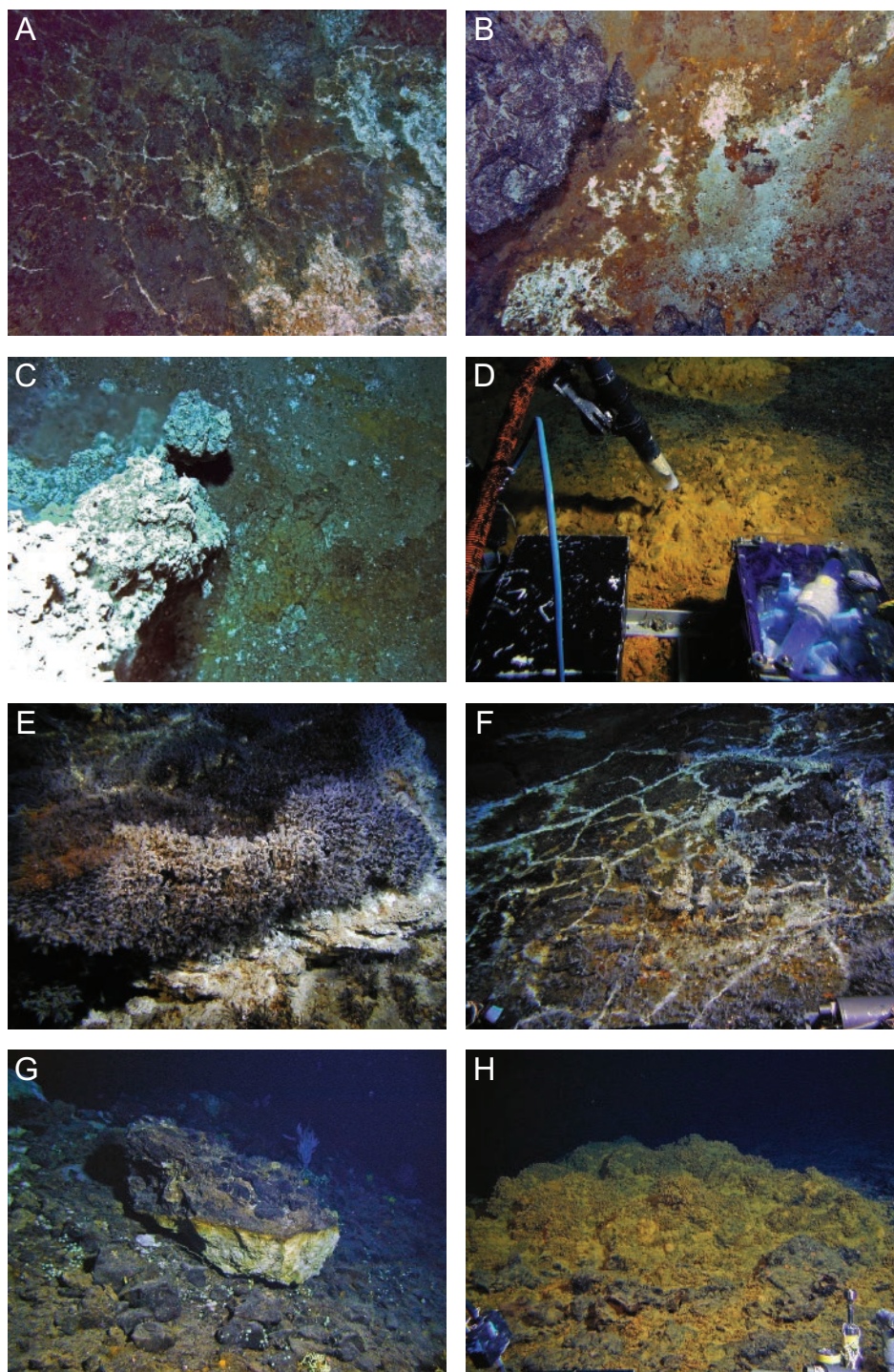
FIG. 8. Evidence for hydrothermal activity seen on the seafloor of the NE cone, Clark volcano. A. Extensive network of fractures on seafloor along ridge spur discharging diffuse hydrothermal fluid. B. Fe oxyhydroxide precipitates (browns) with sulfate and bacterial mats (white). C. Oblique view looking down on top of an active chimney, possibly the same one depicted in Figure 5, as was taken in same area. D. Abundant Fe oxyhydroxide-silica deposits with low-temperature fluid emanating from small mounds. E. Thick accumulations of the long-neck barnacle *Volcanolepas osheai* associated with diffuse venting flowing from layered volcanic rocks. F. Clear, shimmering hydrothermal fluid can be seen discharging from small (up to 30 cm tall) barite-rich chimneys and a network of cracks on the seafloor, near the northern peak of the NW cone. G. Example of thick (≥20 cm) barite-rich crusts that are up to ~19,000 years old (see text). H. Several moundlike structures were seen atop the NW cone summit, commonly covered by long-neck barnacles, indicative of active diffuse venting. These mounds are thought to represent the base of much older chimney structures. (C)-(F) were all taken within a few 10s of meters of the Twin Towers chimneys, while (G) is located ~140 m northwest, and (A) 30 m and (H) ~80 m south-southeast of the chimneys, respectively (see Fig. 4A for locations). (A)-(C) were taken by *TowCam* during tow TC01; (E)-(H) during *Pisces* dive PV-623, and (D) during PV-634. Standard Photoshop CS5® corrections for tone, contrast, and color were used on the images.
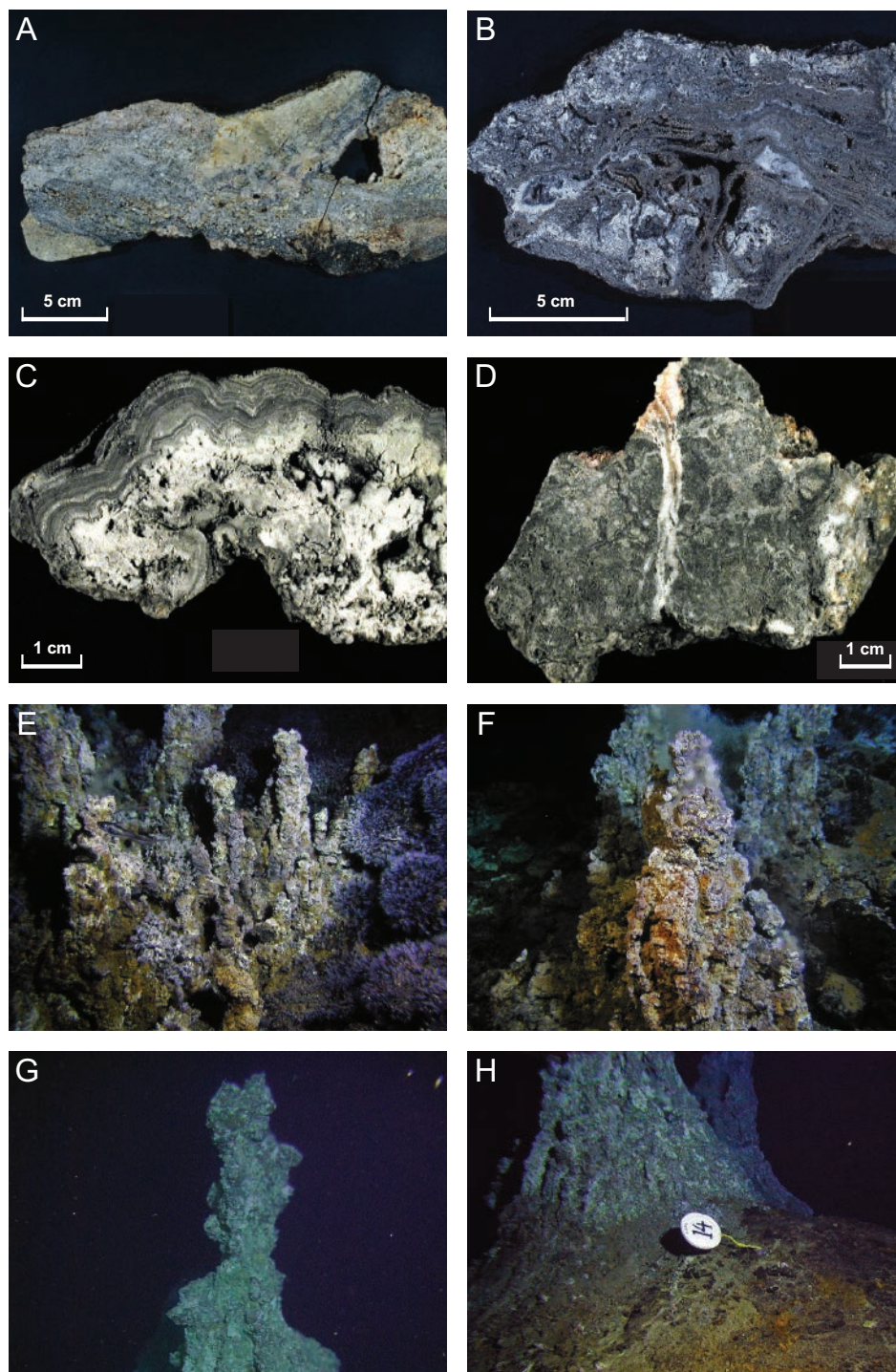
FIG. 9. A. In part laminated, locally reworked crust (sample SO135-74DR-1); clasts silicified and clay altered, and occasionally altered to a green color while the exterior of the sample is coated by Mn oxide. The matrix is dominated by barite. This sample is ~19,000 yrs old (see Table 3). B. Slice through the "fisherman" sample (referred to as 74DR-12 in Tables 2–4, and Clark-1 to -4 in Table 2), which is dominated by anhydrite with gypsum and barite, and lesser pyrite ± marcasite. C. Barite-anhydrite crust with pyrite-rich laminations and a botryoidal outer surface. D. Mineralized breccia sample showing evidence for later vein of silica + barite in a barite-pyrite matrix. E. Small, up to 30 m high, delicate chimneys comprised mostly of sulfates discharging hydrothermal fluids between 56° and 106°C; commonly associated with clusters of long-neck barnacles. F. Close-up on one of these delicate chimneys where clear fluid emanates from the top of the chimney. G. Top of one of the Twin Towers chimneys showing a bulbous exterior. H. Base of the same Twin Towers chimney, which is perched on top of a sulfide mound with Mkr-14 deployed in the foreground. Photographs (E) and (H) were taken by the Twin Towers chimneys, while (F) and (G) were taken in close proximity (see Fig. 4A for locations). Photographs (F)-(H) were taken by *Pisces V* during dive PV-623 and (E) during PV-634. Standard Photoshop CS5® corrections for tone, contrast, and color were used in the images.
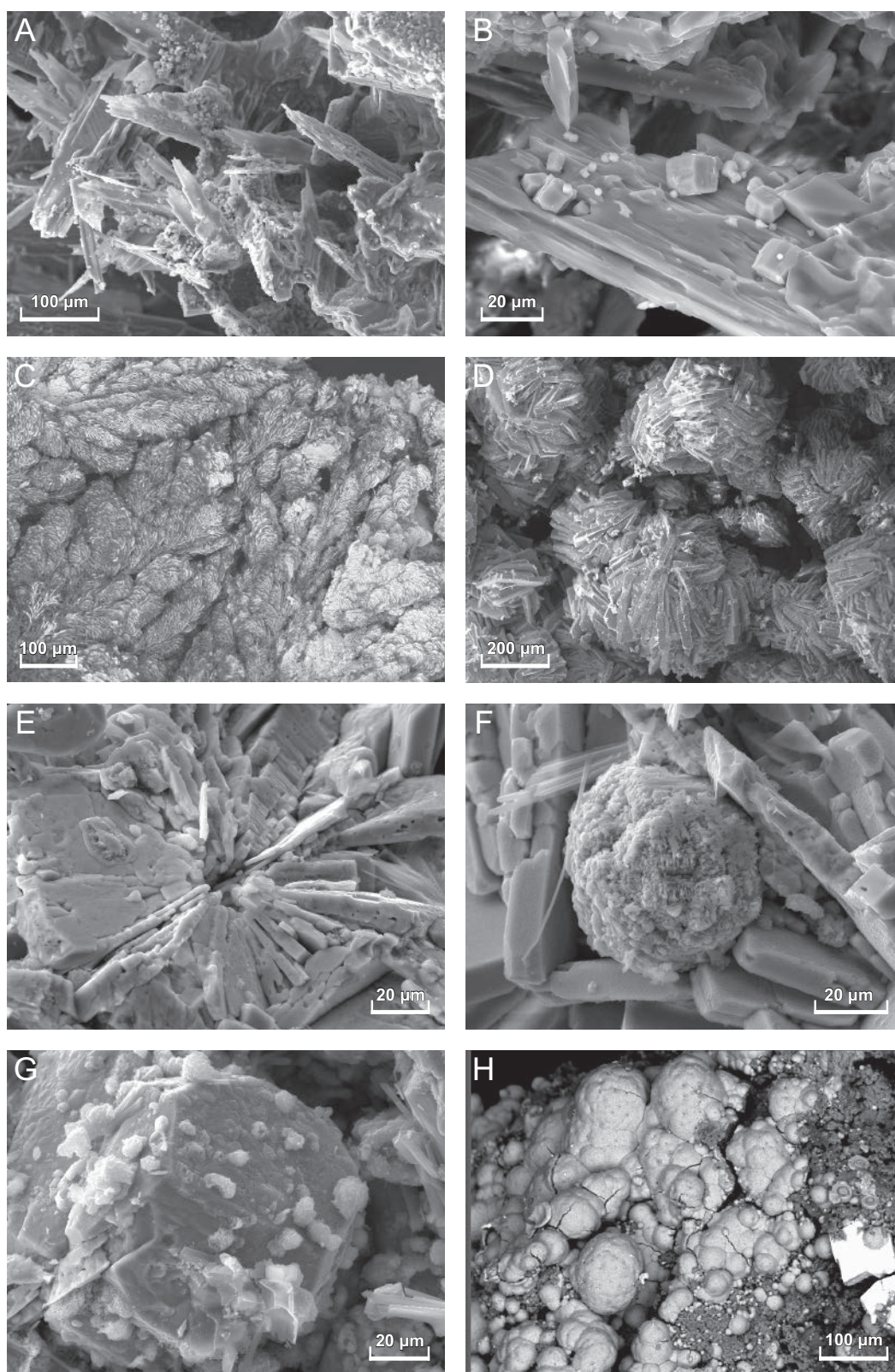
FIG. 10. SEM images of select Clark chimney samples. A. Blades of anhydrite from a Twin Towers chimney sample (PV623-8R). B. Anhydrite covered with grains of pyrite (PV623-8R). C. Barite fronds typical of quenching (i.e., mixing between hydrothermal fluid and seawater) from one of the "fisherman" chimney samples (Clark-4b). D. Lepispheres, or balls of barite laths (SO135-74DR-12-3). E. Typical radial, or rosette habit of barite commonly seen in the sulfate-dominant chimneys from Clark (SO135-74DR-12-1). F. Botryoidal pyrite intergrown with barite laths (SO135-74DR-12-1). G. Euhedral pyrite covered by small blebs of opal (SO135-74DR-12-1). H. Colloform Mn oxides coating anhydrite (Clark-1c).

FIG. 11. A. REE data for Clark mineralized samples (Appendix 2B) and select volcanic rocks. As there are no REE concentrations of apatite for the Kermadec arc, the I-type granite of Chu et al. (2009) has been used. The only reported REE contents from Kermadec arc plagioclase is that of Saunders et al. (2010) for one plagioclase from Healy volcano. Thus, the plagioclase compositions shown are of two plagioclases of differing anorthite composition from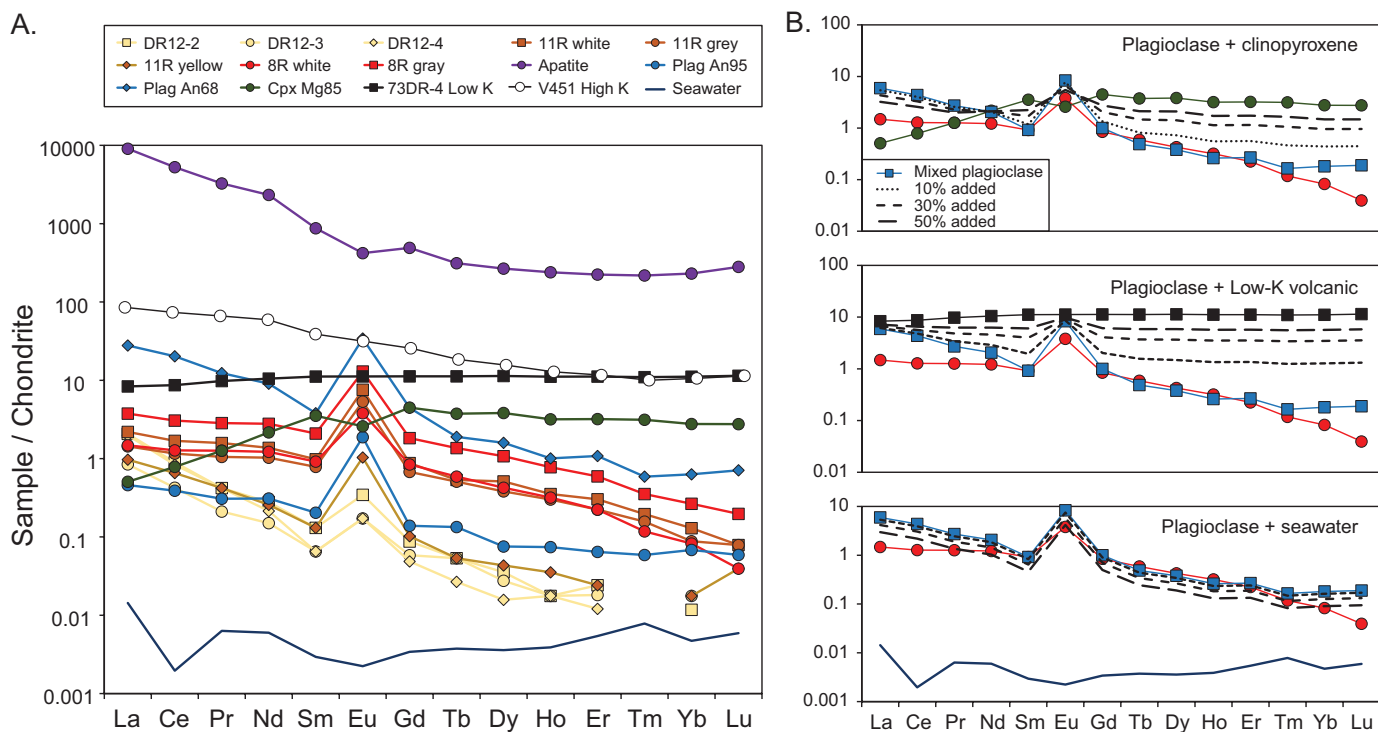 Honshu, Japan (Tatsumi et al., 2008). The low K sample 73DR-4 is from Haase et al. (2002) and the high K sample V451 from Wysoczanski et al. (2012), both from Clark volcano. The clinopyroxene composition is from Barker et al. (2012), while the seawater data were taken from http://www.webelements.com/periodicity/abundance_seawater, and the chondrite normalized data from Sun and McDonough (1989). Samples 8R- and -gray, and 11R-white, -gray and -yellow are subsamples from different alteration zones within those samples, respectively. B. Modeling of plagioclase with variable amounts (10, 30, and 50%) of clinopyroxene, melt, and seawater. The (Honshu) plagioclase composition used is a mixture of 80% An95 with 20% An65. This reflects the average composition of plagioclase in Clark low K rocks from mineral chemistry and proportions given by Gamble et al (1997).

in the pyrite-rich samples (up to 7,430 ppm), as are Sb (up to 219 ppm), Hg (up to 1,170 ppm), and Tl (up to 115 ppm); base metals are only 10s to 100s of ppm in these samples, typically with Pb > Zn > Cu. An anhydrite-rich sample has the highest Cu content (974 ppm), and a silica-clay sample the highest Zn (3,860 ppm), and Pb (1,240 ppm). The average Au content is 2.9 ppm for all the mineralized samples and 8.1 ppm Au for the seven subsamples analyzed from the pyrite + marcasite-rich zones within the "fisherman" sample (i.e., SO135-74DR12-1 to -4 and Clark-4A, -4B1 and -4B2; Appendix 2A). The pyrite and marcasite are mainly stoichiometric FeS_2, with up to 1.1 wt % As (not shown). A number of samples are enriched in Si, Al ± Mg, K, and Zr and are probably related to the presence of altered volcanic clasts and/or clay minerals.

Trace element geochemistry of mineralized types

Using the above-mentioned mineralization types, the following summary is made of their trace element signatures (see Appendix 2A, B; Fig. 11).

Barite-rich samples: These samples mostly show no significant trace element enrichments (except Sr substitution for Ba), although one sample (P5-634-3R) has a Zn content of 1,440 ppm. Of the REEs, only La, Ce, Pr, Nd, and Tb are present above detection limits.

Barite-pyrite samples: These samples contain As, Pb, Zn, Ag, Sb, Hg, Tl, and Au (i.e., the "epithermal" suite of elements) in notable amounts; within this sample suite, the contents of Au, Ag, As, and Sb generally correlate with the abundance of pyrite. One of the fisherman subsamples contained a distinct black barite band with disseminated pyrite-marcasite that yielded 15.1 ppm Au (e.g., Clark-4B-2; cf. Fig. 9C). The LREE are present in near to slightly enriched chondritic abundances, whereas the HREE are not present in measureable amounts. An apparent negative Sm anomaly in the REE patterns is probably due to very low Sm abundances and high Eu, suggesting a strong positive Eu anomaly.

Barite-anhydrite samples: These samples contain up to 960 ppm Zn, consistent with traces of sphalerite seen by petrography, together with up to 470 ppm Pb and 2.6 ppm Au. The REE show LREE enrichment relative to HREE (La/Yb up to 50) with distinct positive Eu anomalies.

Anhydrite-rich samples: These samples also have significant Au contents up to 2.3 ppm, with similar Au/base metal values to the barite-rich samples, but less than those of the barite-pyrite samples (Appendix 2). LREE contents range from chondritic to enriched (up to 10×) and HREE from chondritic to below detection limit, with moderate to strong positive Eu anomalies.

Silica samples: These samples had trace elements mostly below detection limits.

Fe-Mn-silica samples: These samples contain abundant Al, Mg, Na, K, P, U, Th, and Sc, possibly related to minor clays (e.g., smectite) and adsorbed cations, and sorption from seawater. The highest contents for Co, Mo, and Ni appear to correlate with high Fe and Mn, most likely reflecting adsorption onto Fe-Mn oxyhydroxides. Traces of Ga are common in this type of sample and are associated with Si phases, or clays. REE patterns are generally flat and above chondritic values, with positive Eu anomalies.

Silica-clay samples: These samples are characterized by high concentrations of Si, Al, Mg, Na, K, Rb and traces of Ti, Zr, Y, Sc, U, Th, typical of altered volcanic material and/or clay-rich mineralization. Traces of Ga are also common in this type of sample and are also associated with Si phases, or clays. One sample (SO135-74DR6) contains relatively high Zn, Pb, and Au.

Barite-silica-clay samples: These samples have bulk chemistry similar to the silica-clay samples, containing up to

30–45 wt % BaO. Clays are inferred to be Mg smectites (see above). The one sample analyzed for REE shows a strong enrichment of LREE over HREE, the latter being close to detection limits.

Element scans

Mineral element mapping provides a link between mineralogy and bulk mineralization geochemistry. The dominance of sulfates in the walls of the Twin Towers chimney (Fig. 12; PV623-11R) are apparent in the element scans, with S, Ca, and Ba maps outlining laths of anhydrite ($CaSO_4$) and fronds of barite ($BaSO_4$). The distribution of these elements highlights the intergrowth of these sulfates, resulting in the patterns commonly associated with sulfate-rich walls within chimneys of Kermadec arc hydrothermal systems (e.g., Brothers volcano; de Ronde et al., 2005; Berkenbosch et al., 2012) and elsewhere (e.g., Bikpela chimney of the PACMANUS hydrothermal field, Papua New Guinea; Binns, 2014), where mixing has occurred between hydrothermal fluid and seawater. Strontium correlates with barite while the distribution of
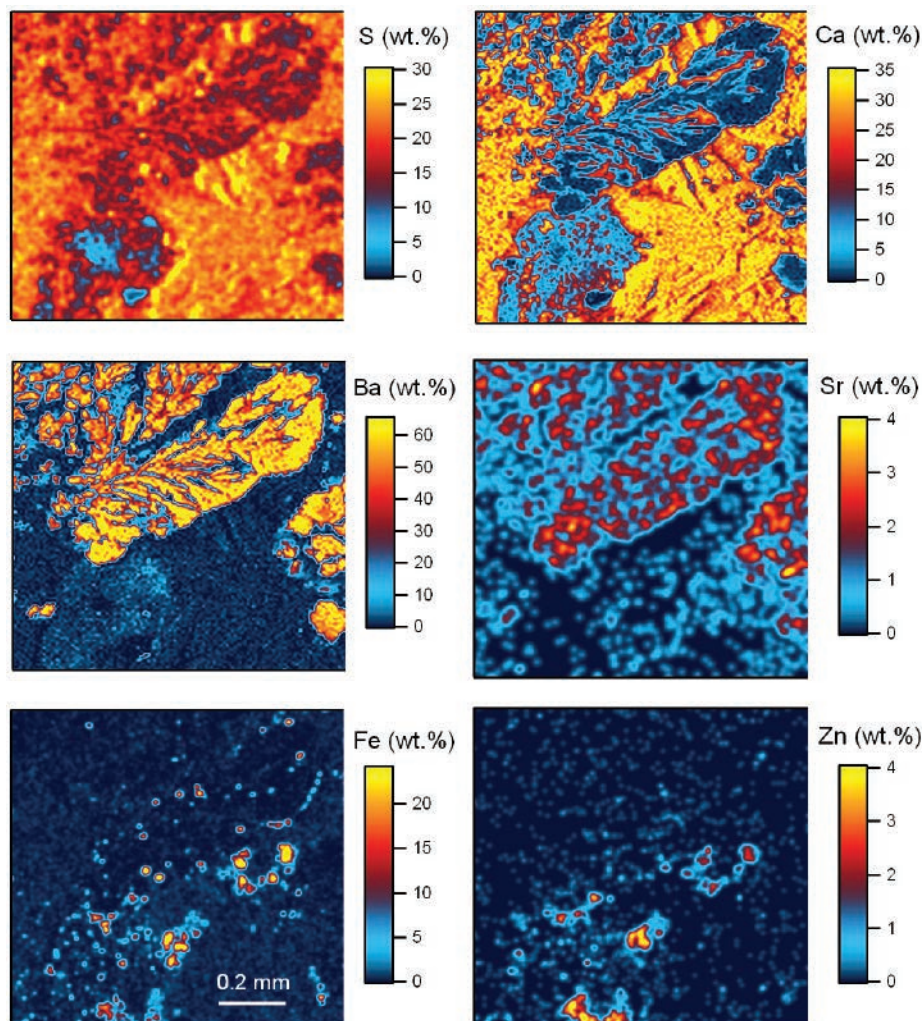

FIG. 12. PIXE element scans for sample PV623-11R collected from near the base of the Twin Towers chimney site (see Fig. 9H). The scans each represent an area 1 mm². The raw map data of X-ray counts, as a function of position, have been converted to semiconcentration values by extracting calibration values from a quantitative analysis of the sum X-ray spectrum for the whole map.

Fe and Zn highlight minor pyrite and sphalerite phases in the sample. Scans made from other chimney samples also show minor Si, and more rarely Pb, the former relating to the opal seen in the SEM studies (Fig. 10) and the latter minor galena in the sulfides (see above).

Sulfur and oxygen isotopes

Barite (n = 4) and anhydrite (n = 5) were analyzed from barite-silica-clay and massive anhydrite samples, while these sulfates and pyrite were also analyzed from the fisherman sample (Table 2). Values of $\delta^{34}S_{anhydrite}$ range from 20.0 to 23.7‰ (avg 21.5‰) while values of $\delta^{34}S_{barite}$ range 18.2 to 20.2‰ (avg 19.6‰), or similar to seawater values (~21‰; Paris et al., 2013). As there is minimal fractionation between sulfate minerals and aqueous sulfate, the measured isotopic composition of sulfate minerals approximates the isotopic composition of the parent fluid (Seal et al., 2000, and references therein). Thus, the results given in Table 2 indicate that barite and anhydrite were both formed by mixing of Ba- and Ca-rich hydrothermal fluids with seawater.

Values of $\delta^{34}S_{pyrite}$ (n = 6) range from 2.0 to 3.7‰ (avg 2.6‰). The most favorable conditions for isotopic exchange in typical hydrothermal systems are temperatures above ~200°C, near-neutral to slightly acidic conditions (i.e., pH ≈4–7), and ΣS =10^{-2} m (Ohmoto and Lasaga, 1982). We can therefore calculate temperatures of formation from the sulfur isotopic compositions of coexisting mineral pairs. Values of $\delta^{34}S_{anhydrite-pyrite}$ range between 19.0 and 21.7 for the fisherman chimney samples. Combining the fractionation factors for SO_4 minerals and aqueous sulfate (Ohmoto and Lasaga, 1982) with those of pyrite (Ohmoto and Rye, 1979) and solving for temperature shows $\delta^{34}S_{anhydrite-pyrite}$ values equate to formation temperatures of 228° to 249°C, or slightly higher than the highest measured vent fluid temperature of 221°C.

Oxygen isotope analyses for anhydrite (n = 5) range between $\delta^{18}O$ = 7.1 and 8.6‰ (Table 2), averaging 7.8‰. Values of $\delta^{18}O$ positively correlate with the $\delta^{34}S$ value for the same sample, consistent with isotopic equilibrium between S species and seawater over a temperature range (Robinson, 1977; cf. de Ronde et al., 2005).

Age of Mineralization

Pieces of chimney, crusts, and other barite-rich material have been dated to determine the age of mineralization at Clark, the duration of hydrothermal activity at this volcano, and to compare with ages for mineralization at Brothers volcano, the only other Kermadec volcano to have been dated for mineralization (de Ronde et al., 2005, 2011).

Radiometric ages

Chimney samples collected from focused venting sites were <1.5 years old at time of sampling, with their $^{226}Ra/Ba$ values reasonably consistent, averaging 19.1 ± 0.4 Bq.g^{-1} (Table 3). However, similarly young mineralization from sites where venting was diffuse had variable, and relatively low $^{226}Ra/Ba$ values, i.e., 11.5 ± 0.1 to 16.4 ± 0.2 Bq.g^{-1}, due to radioactive decay. We attribute this difference to the barite being of mixed age. Using a newly developed radiometric technique (Appendix 3), we show how the oldest barite is from an earlier hydrothermal event and has been dissolved and redeposited (see Discussion).

Some of the samples we have dated may be predominantly remnant barite from decomposed chimneys that have been mechanically weathered and dispersed on the seafloor. For example, crust sample PV623-6B-1 contains 50% barite and virtually no sulfide. Sectioning the sample for radiometric dating exposed numerous small vugs and zonation within the massive, cream-colored material (e.g., PV623-6B-1d). Another section (PV623-6B-1c) was host to a vein composed of 12 wt % of fine-grained, white barite, with the remainder silica, that likely coprecipitated during a later hydrothermal event. The $^{226}Ra/Ba$ value for most of sample PV623-6B-1 is 3.45 ± 0.04 Bq.g^{-1}, increasing to 7.22 ± 0.08 Bq.g^{-1} for the upper 1 mm of a relatively soft surface layer, but still well below the initial value of 19.1 ± 0.4 Bq.g^{-1} (Table 3). From the $^{226}Ra/Ba$ values, most of the sample is 3,940 years old whereas the upper 1 mm contains barite of mixed age. The younger component is almost certainly from a hydrothermal event that began within the last few years. That is, radiometric dating using the $^{228}Ra/^{226}Ra$ and $^{228}Th/^{228}Ra$ methods gave discordant ages of 13.3 ± 0.3 and 1.27 ± 0.14 years, respectively, indicating an age gradient through this thin, outer layer.

Sample PV623-6B-2 is from the same area as PV623-6B-1, yet it is different in both appearance and age. For example, its surface has been stained by Fe oxyhydroxide and, as ^{228}Ra is undetectable, there has been no recent mineralization. From the $^{226}Ra/Ba$ values, the barite throughout this sample is 3,230 years old, or 710 years younger than the bulk of PV623-6B-1 (Table 3). We also dated a laminated, partially silicified crust composed of mostly pure barite (SO135-74DR-1; see Fig. 9A; cf. Fig. 8G). Using the estimated initial $^{226}Ra/Ba$ value of 19.1 ± 0.4 Bq.g^{-1}, the calculated age is 19,000 ± 500 years, or considerably older than mineralization ages obtained for any other samples from Clark, or indeed from Brothers volcano (Table 3; de Ronde et al., 2011).

Finally, three subsamples were dated from the fisherman chimney 74DR-12; one from the exterior, one from the

TABLE 2. Clark Sulfide/Sulfate $\delta^{34}S$ and $\delta^{18}O$ Data

Location/Sample no.	Mineral analyzed	$\delta^{34}S$ (‰)	$\delta^{18}O$ (‰)
NW Summit vents			
74DR-1	an	20.0	7.6
74DR-9	an	20.5	7.1
74DR-12-1	py	2.5	
74DR-12-2	an	22.5	8.6
74DR-12-2	py	2.2	
74DR-12-3	an	21.3	7.1
74DR-12-3	py	2.3	
74DR-12-4	an	23.7	8.4
74DR-12-4	py	2.0	
Clark-4a	py	3.7	
Clark-4b	ba	20.1	na
Clark-4c	py	2.7	
Clark-1	ba	18.2	na
Clark-2a	ba	20.0	na
Clark-3b	ba	20.2	na

Abbreviations: an = anhydrite, ba = barite, DR = dredge, na = not analyzed, py = pyrite; all the DR samples are prefaced by "SO-135" (R/V *Sonne* 135 cruise); see Appendix 2 for descriptions of sample types; the 74DR-12 and Clark samples both relate to the "fisherman" chimney sample mentioned in the text; see Appendix 1 for precision and accuracy of the results

TABLE 3. Ages for Mineralized Samples from Clark Volcano

Cruise/ Sample no.	Sample type and region analyzed	Collection date	^{226}Ra Bq·kg^{-1}	^{226}Ra/Ba Bq·g^{-1}	^{228}Ra/Ba Bq·g^{-1}	^{228}Ra/^{226}Ra Bq·Bq^{-1}	^{228}Th/^{228}Ra Bq·Bq^{-1}	% recent barite[1]	Age (yrs) at collection date — Oldest barite component	Age (yrs) at collection date — Most recent mineralization
"Fisherman" chimney										
74DR-12a	Exterior edge	15-Oct-98	10670 ± 30	18.94 ± 0.20	2.10 ± 0.56	0.118 ± 0.002	nm	100.0		18.4 ± 0.3
74DR-12b	Vug lined with barite		10250 ± 30	19.78 ± 0.14	1.65 ± 0.09	0.100 ± 0.002	nm	100.0		19.8 ± 0.3
74DR-12c	Interior-barite rich		3870 ± 10	18.22 ± 0.13	1.34 ± 0.11	0.079 ± 0.002	nm	100.0		21.8 ± 0.3
R/V Sonne 135 cruise										
74DR-1	Silicified barite breccia	5-Oct-98	3.5 ± 1.6	0.006 ± 0.001	nd				19,000 ± 500	
Pisces V cruise										
PV623-3SS	VMS from lava-hosted vent	28 Apr 05	560 ± 5	5.13 ± 0.07	nd				3,040 ± 60	
PV623-4Min	Sediment sulfide and ash	28-Apr-05	7270 ± 30	16.41 ± 0.17	11.73 ± 0.14	0.786 ± 0.006	0.122 ± 0.005	68.5	1,370 ± 250	0.35 ± 0.02
PV623-5SS	VMS from diffuse vent	28-Apr-05	2240 ± 30	11.38 ± 0.13	8.11 ± 0.41	0.768 ± 0.013	0.058 ± 0.010	46.3		0.16 ± 0.03
	Barite-rich crust									
PV623-6B-1a	Soft beige-white surface	28-Apr-05	3890 ± 30	7.22 ± 0.08	1.73 ± 0.08	0.218 ± 0.005	0.397 ± 0.037	11.3	2,790 ± 50	1.27 ± 0.14
PV623-6B-1b	White-cream		2170 ± 20	3.92 ± 0.04	nd				3,660 ± 30	
PV623-6B-1d	Inner		1920 ± 20	3.42 ± 0.04	nd				3,970 ± 30	
PV623-6B-1e	Inner		2010 ± 20	3.40 ± 0.04	nd				3,980 ± 30	
PV623-6B-1f	Inner		1870 ± 20	3.47 ± 0.04	nd				3,940 ± 30	
PV623-6B-1g	Inner		1980 ± 20	3.49 ± 0.04	nd				3,920 ± 30	
PV623-6B-1h	Subsurface		2280 ± 30	3.47 ± 0.04	nd				3,940 ± 30	
PV623-6B-2	Inner, with minor iron stain	28-Apr-05	2390 ± 10	4.68 ± 0.05	nd				3,240 ± 30	
PV623-6B-2	Outer, with strong iron stain		2390 ± 10	4.74 ± 0.05	nd				3,220 ± 30	
PV623-7R	Small venting chimney	28-Apr-05	6800 ± 40	11.66 ± 0.12	9.41 ± 0.16	0.927 ± 0.008	0.138 ± 0.005	55.3	4,740 ± 610	0.40 ± 0.02
PV623-8R	Twin Towers (TT) chimney	28-Apr-05	370 ± 8	18.68 ± 0.29	17.44 ± 0.50	1.102 ± 0.035	0.043 ± 0.019	100.0		0.12 ± 0.06
PV623-11R	Pieces of Twin Towers chimney	28-Apr-05	390 ± 8	16.78 ± 0.25	15.85 ± 0.43	0.973 ± 0.033	0.080 ± 0.024	90.4		0.23 ± 0.07
PV623-17 R/M	Crust: Iron-rich layer	28-Apr-05	530 ± 5			0.061 ± 0.006	0.52 ± 0.18			1.75 ± 0.76
PV623-17 R/M	Crust: White zone		150 ± 2			0.146 ± 0.010	0.36 ± 0.11			1.13 ± 0.41
PV634-3R	Piece fallen off chimney	18-May-05	6520 ± 40	11.48 ± 0.13	7.41 ± 0.12	0.801 ± 0.008	0.361 ± 0.008	47.6	3,540 ± 280	1.14 ± 0.03
PV634-8R	Small chimney	18-May-05	710 ± 10	19.46 ± 0.27	17.88 ± 0.42	1.041 ± 0.027	0.021 ± 0.014	100.0		0.06 ± 0.04
PV634-9R/B-1	White vent (inner) near TT	18-May-05	7830 ± 40	13.44 ± 0.15	6.72 ± 0.13	0.579 ± 0.006	0.400 ± 0.009	44.0	1,740 ± 120	1.29 ± 0.04
PV634-9R/B-2	White vent (outer) near TT		7930 ± 30	14.11 ± 0.15	8.71 ± 0.17	0.706 ± 0.005	0.167 ± 0.005	51.8	1,800 ± 160	0.49 ± 0.02
Initial ratios (highest values for recent mineralization)[2]				19.1 ± 0.4	17.9 ± 0.3	1.08 ± 0.03				

Isotope activities and ages are adjusted to the sample collection date and errors (counting statistics only) are 1σ;
nd = ^{228}Ra below detection limit, nm = not measured

Radiometric dating methods used:

Age (years)	Isotope ratio	Principle
<2	^{228}Th/^{228}Ra	^{228}Ra–^{228}Th disequilibrium
2–30	^{228}Ra/^{226}Ra	Decrease in ^{228}Ra/^{226}Ra value due to the radium isotopes decaying at different rates since the time of mineralization
>300	^{226}Ra/Ba	Decrease in ^{226}Ra/Ba value due to radioactive decay since the time of mineralization

[1] Calculated from the decrease in initial ^{228}Ra/Ba value due to the component of older barite with no ^{228}Ra (decayed); using the % recent barite and the established initial ^{226}Ra/Ba value, the ^{226}Ra/Ba and age of the older barite component can be estimated; does not apply to 100% values

[2] Revised initial values for ^{226}Ra/Ba and ^{228}Ra/^{226}Ra, previously 14.8 ± 2.9 and 0.94 ± 0.14 (Ditchburn et al., 2012)

interior, and a third from a vug lined with barite (Fig. 9B). They had an average $^{226}Ra/Ba$ value of 19.0 ± 0.4 Bq.g^{-1} at the time of mineralization (cf. 22.3 ± 1.7 Bq.g^{-1} for chimneys from Brothers volcano; de Ronde et. al., 2005, 2011). Using $^{228}Ra/^{226}Ra$ values of 0.118 ± 0.002, 0.100 ± 0.002, and 0.079 ± 0.002 Bq.Bq^{-1} derived from each sample, and an initial value of 1.08 ± 0.03 Bq.Bq^{-1}, the ages for the three samples from the chimney exterior to its interior are 18.4 ± 0.3, 19.8 ± 0.3, and 21.8 ± 0.3 years, respectively (Table 3).

Sr-Nd-Pb Isotope Compositions of Clark Chimneys and Lavas

The Clark chimney samples define a generally restricted range in Sr isotope ratios of $^{87}Sr/^{86}Sr$ = 0.705085 to 0.705484, with one sample showing a more radiogenic composition (i.e., $^{87}Sr/^{86}Sr$ = 0.706151; Table 4). These ratios are similar to Clark high K rock samples, with the one chimney sample having a more radiogenic composition trending toward seawater composition ($^{87}Sr/^{86}Sr_{seawater}$ ≈ 0.709; Ling et al., 1997). By contrast, Nd isotope ratios span a wide range from $^{143}Nd/^{144}Nd$ = 0.513155 to 0.51273. Notably, one sample (P5-623-8R-gray) is unusual in having a depleted mantle Nd isotope composition (0.513155) similar to that of the East Pacific Rise (Fig. 13) and is higher than any volcanic sample reported from the Kermadec arc (e.g., Todd et al., 2011), yet has an evolved Sr isotope composition (0.705279). Of the other mineralized samples, three have Nd compositions similar to Clark low K rocks, while two are similar to the high K samples (Table 4). This large range in Nd isotope compositions, when compared to a relatively small range in Sr compositions, suggests a highly heterogeneous source for Nd in the chimney samples, which includes a depleted mantle component.

Chimney Pb isotope ratios show a highly restricted range ($^{206}Pb/^{204}Pb$ = 18.770–18.780; $^{207}Pb/^{204}Pb$ = 15.599–15.603; $^{208}Pb/^{204}Pb$ = 38.657–38.666; Table 4). The general similarity between the Pb isotope composition of the chimney samples and that of the more radiogenic low K lavas suggests that the Pb was mainly derived from the lavas. Importantly, the crusts are distinct in Pb isotope composition from the high K lavas,
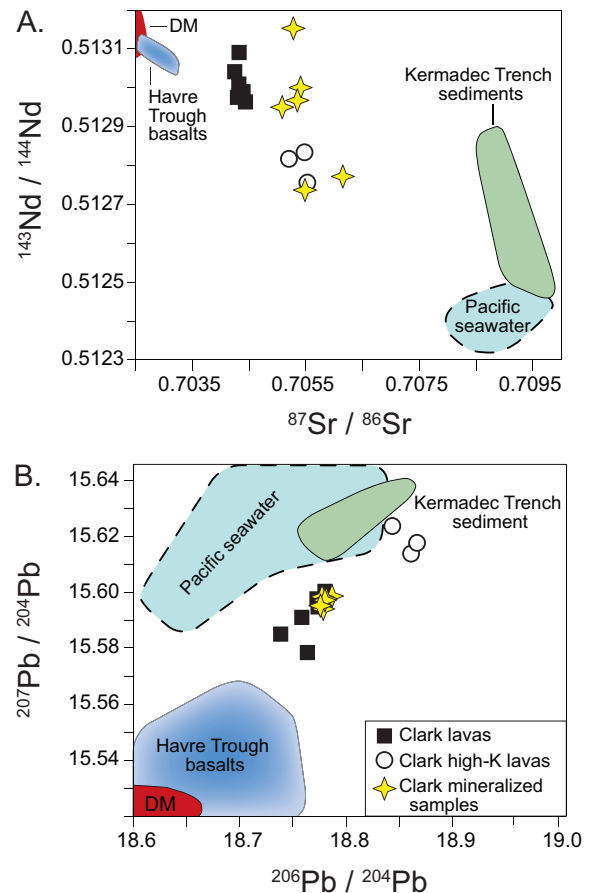

FIG. 13. Radiogenic isotope plots. A. $^{143}Nd/^{144}Nd$ vs. $^{87}Sr/^{86}Sr$. B. $^{207}Pb/^{204}Pb$ vs. $^{206}Pb/^{204}Pb$. In the legend, Clark lavas (black squares) refers to basaltic andesites and one dacite (data from Gamble et al., 1997; Todd et al., 2010; this study Table 4); Clark high K lavas (white circles) refers to basalt (data from Gamble et al., 1997; this study Table 4); Clark mineralized samples (yellow stars) refers to crusts and chimneys (this study Table 4). The field for depleted mantle (DM) is represented by the East Pacific Rise of Meyzen et al. (2007); fields for Havre Trough basalts (Gamble et al., 1996; Haase et al., 2002), Kermadec trench sediment (Gamble et al., 1996; Turner et al., 1997), and Pacific seawater (Ling et al., 1997) are shown for comparison.

TABLE 4. Sr-Nd-Pb Isotope Ratios of Clark Chimney Sulfides, Sulfates, and Lavas

Sample no.	Location-check	Sample type	$^{87}Sr/^{86}Sr$	$^{143}Nd/^{144}Nd$	$^{206}Pb/^{204}Pb$	$^{207}Pb/^{204}Pb$	$^{208}Pb/^{204}Pb$
Chimney samples							
P5-623-11R white	Twin Towers	anhy, gyp	-	-	18.771	15.600	38.659
P5-623-11R gray	Twin Towers	anhy, gyp	0.705408	0.513003	18.780	15.603	38.665
P5-623-11R yellow	Twin Towers	anhy, gyp, ba	-	-	18.774	15.602	38.666
P5-623-8R white	SW of Twin Towers	anhy, gyp, ba	0.705352	0.512970	18.774	15.602	38.664
P5-623-8R gray surf	SW of Twin Towers	anhy, gyp, py	0.705279	0.513155	18.771	15.600	38.661
P5-623-8R yellowish	SW of Twin Towers	anhy, gyp, ba	0.706151	0.512774	18.772	15.599	38.657
SO135-74-DR12-1	Fisherman chimney	anhy, ba, py	0.705085	0.512952	18.770	15.603	38.664
SO135-74-DR12-2	Fisherman chimney	anhy, ba, py	-	-	18.771	15.600	38.661
SO135-74-DR12-3	Fisherman chimney	anhy, ba, marc ± py	0.705484	0.512739	18.770	15.600	38.659
SO135-74-DR12-4	Fisherman chimney	anhy, ba, py	-	-	18.770	15.600	38.661
Lavas							
P74517	Northern cone	Basaltic andesite	0.704248	0.513039	18.752	15.596	38.614
P72932	Northern cone	Basaltic andesite	0.704431	0.512965	18.767	15.600	38.654
C3	Northern cone	High-K basalt	0.705527	0.512756	18.854	15.618	38.751
C6	Northern cone	Basaltic andesite	0.704330	0.512975	18.756	15.583	38.520

Notes: anhy = anhydrite, ba = barite, gyp = gypsum, marc = marcasite, py = pyrite; dash means not analyzed

seawater, and depleted mantle, suggesting that little or no Pb in the chimneys is derived from these sources.

The varied isotopic composition of the chimney samples, with both homogeneous Pb ratios, and highly varied Nd ratios, suggests a complex origin for these samples from multiple sources with highly distinct Sr, Nd, and Pb abundances. The nature of these sources will be investigated in the discussion.

Discussion

Regional-scale effects on Clark volcano

Volcanoes of the Kermadec active arc front are in a constant struggle between tectonism and volcanism, with Clark volcano no exception. For example, the two Clark volcanic edifices show the results of these competing processes, with the SE cone dominated by extension and faulting, while the NW cone shows that recent volcanism is prevalent (Fig. 1C). Regional magnetic data highlight these edifices and other volcanic features in the backarc, while regional gravity data show an apparent linear trend of increasing values of mGal toward the NW (Fig. 14); this may reflect subduction of the large Hikurangi plateau westward beneath the Havre trough. Higher resolution geophysical surveys (i.e., more closely spaced lines) show Clark as a whole is magnetized, in concert with volcanic host rocks (Fig. 3A). By contrast, similar resolution gravity surveys show that a steep gradient occurs between the two cones (Figs. 3C, 14C).

We have modeled the gravity gradient and found the best fit to the observed data is achieved by inserting a major, vertical fault between the two edifices (Fig. 15). Projecting to surface would therefore suggest a tectonic boundary separates the NW cone from the SE cone. Given that images derived from
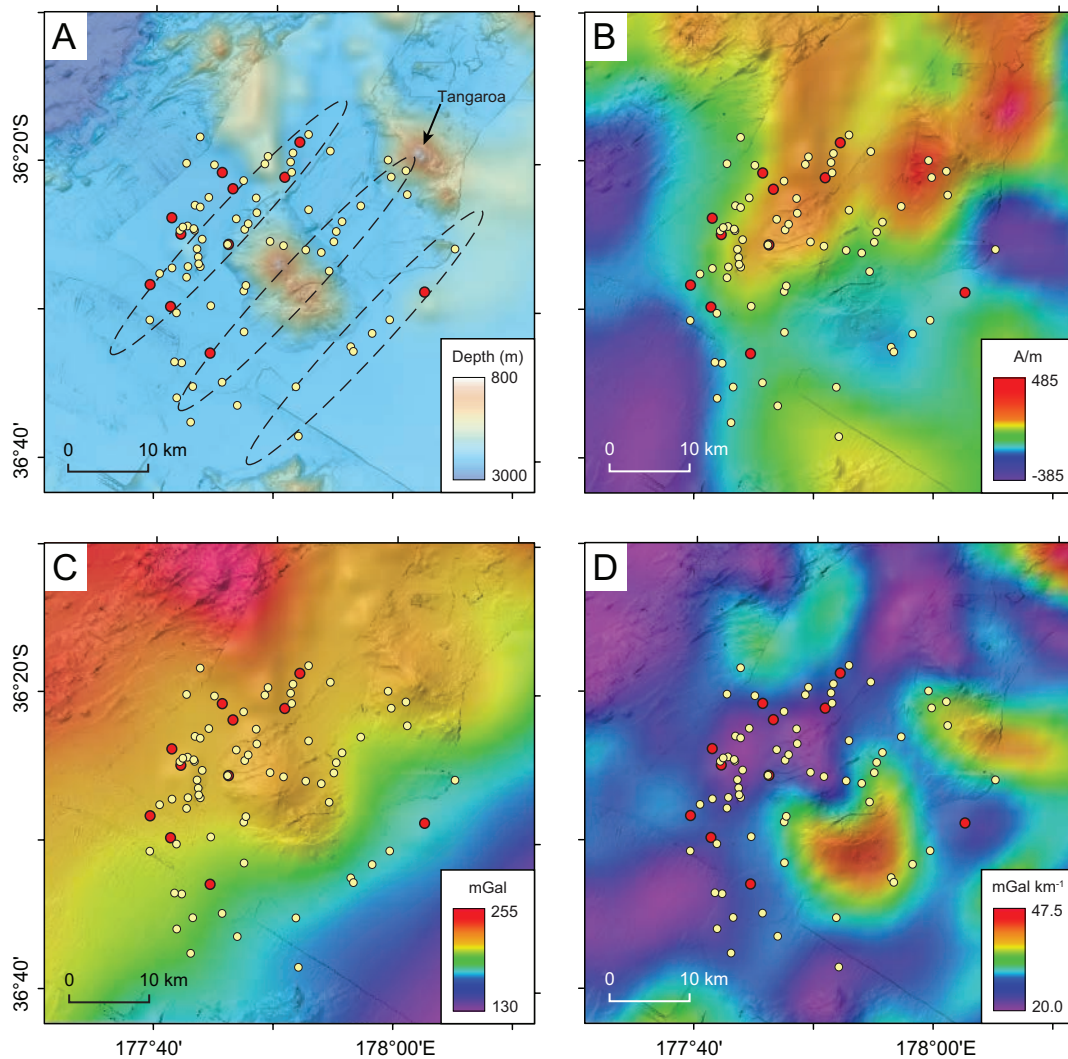
FIG. 14. Regional geophysics in the region of Clark volcano. A. Location of earthquake epicenters. There is a suggestion of a ~NE-SW orientation of the locations, shown spaced 11 km apart, with one group bisecting the two volcanic edifices at Clark where we propose a large crustal-scale fault exists (see Fig. 15). This group of earthquake locations also projects northeastward toward Tangaroa volcano. Shallow earthquakes of uncertain depth are routinely assigned to either 5 or 12 km. Red dots = epicenters of 12-km earthquakes; yellow dots = epicenters of 5-km earthquakes. B. Regional magnetic data for the same region with the volcanic edifices prominent. C. Regional gravity data showing a decrease in values of mGal toward the southeast. D. Gravity gradient map of the region that highlights the gradient between the NW and SE cones of Clark volcano.
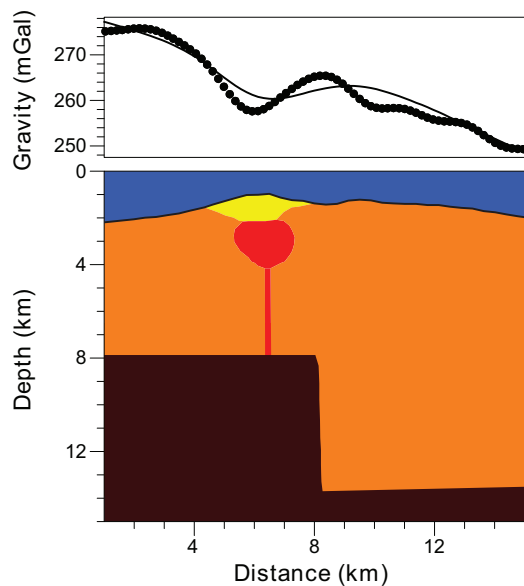
FIG. 15. Clark gravity model. Bold dotted line in the top panel is the observed gravity while the thin solid line is the calculated gravity from the model below. Our preferred interpretation of the observed gravity gradient between the NW and SE cones of Clark (see Fig. 3B) is a major fault occurring between these two edifices. The dip in the observed gravity profile relates to the hydrothermal system and inferred caldera infilling of the NW cone (see Fig. 17). Colors in the model are as follows: blue = seawater (density 1.03 g cm^{-3}); yellow = hydrothermally altered crust (2.0 g cm^{-3}); orange = oceanic crust (2.7 g cm^{-3}); red = magma chamber (2.3 g cm^{-3}); brown = upper mantle (3.2 g cm^{-3}). Vertical exaggeration = 0.83.

towed cameras (Fig. 2) and material recovered in dredges show similar volcanic rocks occur on both cones, consistent with the magnetic data, and that the projected fault is oriented subparallel to the steepest part of the SE cone graben's northern boundary (~053°; Fig. 1C), we believe that this is a crustal-scale fault, with the NW cone underlain by 6 to 7 km of crust and the SE cone 11 to 12 km of crust (Fig. 14).

An alternative scenario to explain the gravity gradient would be to insert a wedge of crustal material, thickening toward the southeast, which would be consistent with the subduction of the Hikurangi plateau. However, plotting the location of both shallow (5 km) and deeper (12 km) earthquake epicenters for the region suggests a trend toward ~045° (Fig. 14A). That is, if we draw an envelope encompassing the earthquake epicenters centered on the inferred fault bisecting the two cones at Clark, we see it projects toward the northeast, or toward the summit of nearby Tangaroa volcano that is also hydrothermally active (Fig. 14A). Using the same orientation, a similar envelope encompasses all the epicenters trending in the same general direction ~11 km southeast of Clark. Finally, constructing a third envelope centered 11 km northwest of Clark encompasses a significant number of epicenters also oriented along a northeast-southwest trend, suggesting that regional-scale tectonism is responsible for extension in the area and likely accounts for volcano locations and their associated hydrothermal systems.

Volcano-scale effects on the Clark hydrothermal system

Regional faults in the vicinity of Clark volcano are responsible for the graben structures that cut both cones, and likely the

emplacement of fissure ridges such as that seen on the northeast flank of the NW cone (Fig. 1C). The SE cone is certainly more degraded than the NW cone, having suffered major sector collapse and is thus considered older; no significant evidence exists there for present-day hydrothermal activity.

The younger, NW cone is characterized by a largely intact edifice, albeit with the onset of sector collapse and graben formation apparent (Fig. 4A). The summit of this cone has two peaks linked by a ridge spur. Towed cameras show rocks in this area are dominated by massive and/or blocky lava flows, talus, and volcaniclastics (Figs. 2, 5). A high-resolution magnetic survey over these peaks shows that the flanks of the edifice appear to cover a slightly oblate (max diameter ~1.8 km) feature that is strongly magnetized (Fig. 4C). We think that this feature represents an earlier caldera structure that has since been filled by lavas and volcaniclastics. The magnetic data also show numerous burn holes, or weakly magnetized zones in the rocks sitting within the oblate feature, marking an overall magnetic signal patterned like Swiss cheese. Closer inspection of these burn holes shows the head scarps of the two sector collapses coincide with magnetic lows, thus the magnetic anomalies could be due to heterogeneous magnetization as a result of mass wasting of the volcanic rocks. However, these areas and the summits of the two peaks also correspond with areas of known hydrothermal activity (Fig. 7). By contrast, three noticeable areas of burn holes to the north, northwest, and west of the peaks do not coincide with any slumps (Fig. 4A) and are also not associated with present-day venting. We believe, therefore, that all the burn holes are consistent with hydrothermal upflow zones, although some of them are inactive today. Individual burn holes that sit immediately inside the walls of the inferred caldera at Clark resemble "donut" shapes; similar magnetic patterns have been reported for the Brothers caldera volcano where they coincide with active vent fields perched on the caldera walls, above ring faults (Caratori Tontini et al., 2012). Thus, either the hydrothermal system at Clark has migrated southeastward to its present position atop the peaks and adjacent slopes, or the outer burn holes represent an episode of hydrothermal activity related to an earlier formed caldera that has since been buried. If true, then the magnetic data captured a change in both volcano growth and hydrothermal system permeability, transitioning from more focused permeability related to caldera ring faults, to more distributed permeability coincident with cone building. This would imply that the hydrothermal system at the NW cone was once bigger, and more active, than today.

Isotope geochemistry

Isotopic compositions of mineralized (crust and chimney) samples show a range in composition, suggesting a complex origin from multiple sources that could include depleted mantle, low and high K lavas, and seawater. Gamble et al. (1997) previously interpreted volcanic rocks from Clark as being sourced from originally depleted mantle (i.e., ambient mantle was present) enriched by fluids, together with some melts derived from the subducting slab, with the high K lavas having a higher sediment component than the low K lavas. Our results are consistent with this interpretation; the origin of the mineralized samples and nature of these sources is modeled in Figure 16.
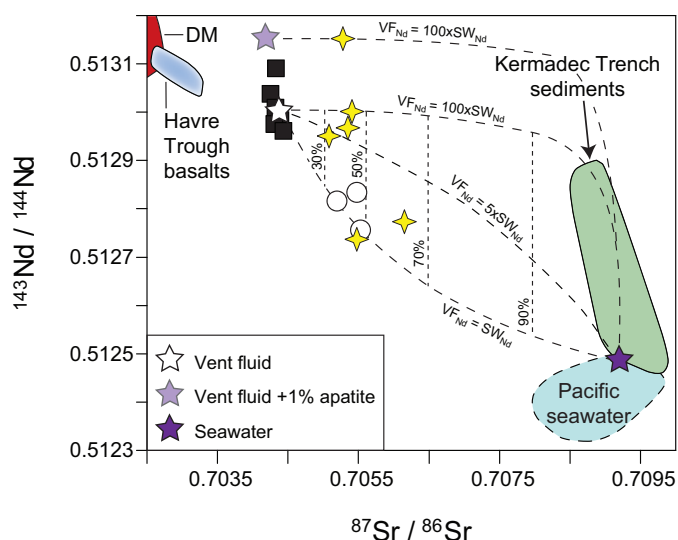
FIG. 16. Isotopic modeling of Clark mineralization. Mixing (dashed) lines are between a vent fluid (white star) and modern seawater (purple star) with the proportion of seawater shown on vertical dashed lines. Nd concentrations of the vent fluid vary from seawater (0.0028 ppb) to 100× seawater; mixing curves for a vent fluid with seawater, 5 and 100× seawater Nd compositions are shown. Sr concentration of seawater used is 8 ppm. The vent fluid is modeled with 25 ppm Sr, or ~3× that of seawater, which is the maximum Sr content measured from Brothers volcano vent fluids (de Ronde et al., 2011). We use the isotopic composition of the low K lavas for that of the vent fluid as they have similar Pb ratios (Gamble et al., 1997; see Fig. 13B); the isotopic composition for the field of "Pacific seawater" is derived from the rims of Mn nodules ranging in age from 200 k.y. up to 57 m.y. (Ling et al., 1997). The mauve star indicates a vent fluid source with 0.075% apatite added (with Nd = 1,000 ppm, Sr = 340 ppm, and an isotopic composition of $^{87}Sr/^{86}Sr$ = 0.7035 and $^{143}Nd/^{144}Nd$ = 0.5132), reflecting enriched depleted mantle (DM). Mixing is shown between the apatite-enriched vent fluid source (where Nd is 100× that of seawater) and seawater. Symbols for high and low K lavas and mineralized samples are the same as in Figure 13.

Despite the mineralized samples having Sr isotope ratios similar to high K lavas, the Pb isotope ratios indicate a source from low K rocks (Fig. 13). That is, because Pb concentrations are greater in high K lavas, any high K component in the chimneys would result in more radiogenic Pb, resulting in trends toward high K compositions. Similarly, any significant depleted mantle (DM) component in the mineralized samples would result in Pb isotope compositions trending toward this field in Figures 13 and 16. Modern seawater, however, has very low Pb concentrations (0.03 ppb; see http://www.webelements.com/periodicity/abundance_seawater) so no amount of seawater added to a host lava component would change the Pb isotope signature. Therefore, Pb in the chimneys is substantially derived from low K host lavas and can be used to fingerprint this component. A host lava source for Pb has similarly been proposed for Conical Seamount and mid-ocean ridge-type mineralization (Fouquet and Marcoux, 1995; Kamenov et al., 2005).

The Sr isotope composition of the mineralized samples can be modeled by mixing between vent fluids derived from low K host lavas and modern seawater. The amount of seawater required is dependent on the Sr content of the vent fluid, with ~40% seawater (65% for one sample) required for a vent fluid with 25 ppm Sr (de Ronde et al., 2011). A vent fluid with even lower Sr concentration will similarly require a lower seawater component (e.g., ~30% for fluid with 16 ppm Sr).

This mixing model can also account for the observed Nd isotope ratios of the mineralized samples but requires a vent fluid with variable Nd concentration (ranging from 1–200× seawater Nd concentrations). This variation in Nd concentration may be the result of Nd precipitating out of the vent fluid at an early stage (i.e., in an Nd-rich mineral phase). One sample, however, that cannot be readily explained by this model is P5-623-8R (gray surface) with its high Nd isotope ratio similar to that of depleted mantle (Fig. 16). Addition of melt or fluid derived from this source can be discounted, as the Sr and Pb isotope composition of the mineralized samples would show a depleted mantle component, but they do not. Any depleted mantle component would have to have low Sr and Pb contents, but a high Nd content, to impart a primitive Nd isotope ratio on the sample without affecting the Sr and Pb isotope ratios. One possible phase is apatite, which is highly enriched in Nd and which has low contents of Sr and Pb. Addition of <<1% of apatite derived from a depleted mantle source would increase the Nd isotope ratio of the vent fluid to that of depleted mantle but not affect Pb isotope compositions, with Sr ratios derived from mixing of the apatite-enriched source (mauve star, Fig. 16) with 40% seawater.

In summary, isotopic compositions for chimney and crust samples indicate mixing of ~40% seawater with a vent fluid derived from low K lavas, with a small addition of a depleted mantle component rich in Nd (possibly apatite). A high K source can be discounted.

REE

The range of REE abundance and distribution patterns observed in seafloor hydrothermal fluids is thought to depend on a number of variables, such as fluid composition (pH, ligand concentration), temperature, and the alteration mineralogy of the host rocks (e.g., Craddock et al., 2010). Studies show that high-temperature (>230°C), low pH (<6) hydrothermal fluids from basaltic mid-ocean ridges have chondrite-normalized REE distribution patterns with LREE enrichment and strong positive Eu anomalies (e.g., Michard et al., 1983; Campbell et al., 1988). It has been suggested that these patterns are linked to the high-temperature alteration of plagioclase during leaching of the host rocks (e.g., Klinkhammer et al., 1994). By contrast, vent fluids from ultramafic-hosted mid-ocean ridges and backarc hydrothermal systems show a range in REE distribution patterns, considered a result of heterogeneous solubility and mobility of the REE during fluid-rock interaction, and the formation of a variety of complexes (e.g., Cl^-, F^-, and SO_4^{2-}) with different aqueous stabilities (Craddock et al., 2010; Schmidt et al., 2010). Thus, the hydrothermal precipitates can either mimic the REE distribution pattern of the vent fluid, or they can fractionate the fluid REE resulting in different patterns (e.g., Dekov et al., 2013).

We suggest that sulfates analyzed in this study are unlikely to have fractionated the REE, with the exception of Eu. For example, in the relatively high temperature (~220°C), low pH (4.9) fluids being expelled on the seafloor at the NW cone, Eu occurs as Eu^{2+}, unlike other lanthanoids that are trivalent under these conditions. The ionic radius of Eu^{2+} (1.09 Å) is close to that of Ca^{2+} (0.99 Å) and to a lesser extent Ba^{2+} (1.35 Å) and thus can easily substitute for them in the Ca and Ba sulfate (anhydrite and barite) crystal lattices. By this mechanism,

sulfates (in particular anhydrite) commonly seen at Clark and other submarine arc seafloor vents can preferentially include Eu in their crystal lattice, accentuating the initial positive Eu anomaly of the parental fluid. While we might expect anhydrite to be a better Eu sink than barite, due to the similarity of the Eu and Ca ionic radii, the REE distribution patterns for Clark sulfates do not differ substantially from each other, irrespective of the different proportions of anhydrite and barite contained within the samples (Fig. 11A). This then suggests that REE fractionation controlled by crystallography has not played a major role during sulfate precipitation. That is, the sulfates most likely reflect the REE distribution patterns of the parental hydrothermal fluid.

The REE distribution patterns of the Clark sulfates, however, differ from those of the inferred host rocks. That is, Clark rocks show REE patterns that are slightly enriched in LREE and have a weakly negative, or no Eu anomaly (Fig. 11A). Conversely, the patterns are very similar to plagioclase, which is enriched in Eu. This suggests that the low K source component identified from isotopic compositions of the mineralization (see above) is derived from plagioclase, which is abundant in low K basaltic andesites (Gamble et al., 1997). Plagioclase is conspicuously absent from the high K samples (Gamble et al., 1997), which would explain the lack of high K-derived isotopic compositions. The potential apatite source for the Nd mentioned above could thus be derived from basement rocks, possibly occurring as inclusions of An-rich plagioclase xenocrysts entrained in the low K lavas.

Large proportions of other low K phases (i.e., glass, or clinopyroxene) can be discounted as a source of leached phases, as they would significantly change the REE patterns of the vent fluid (and mineralized samples). For example, addition of >10% clinopyroxene to plagioclase (Fig 11B) would result in significantly higher HREE than observed. Similarly, 10% of melt (or glass/groundmass) would increase all REE concentrations dramatically and result in a flat pattern, resembling the host rocks. Addition of seawater will not change REE concentrations, or normalized patterns, even with up to 70% added (the maximum suggested from Sr isotopes), consistent with isotopic modeling requiring a significant addition of seawater (Fig. 11B).

The source of the vent fluid is best explained then, as being derived from the dissolution of plagioclase in low K host lavas with <10% total of other host lava phases, such as clinopyroxene, glass, or groundmass. This component then mixes with ~40% seawater. The generally lower HREE content of the mineralized samples compared to plagioclase suggests incomplete dissolution and LREE preferentially scavenged from plagioclase by the vent fluid. This is expected, as LREE are more mobile in hydrothermal fluids than are HREE. Again, a source derived from high K lavas can be discounted.

Mineralization

Hydrothermal activity at Clark is dominated by low-temperature, diffuse venting seen emanating from cracks, fissures, and along bedding planes of volcaniclastics, and manifest by plentiful crusts, Fe-Si-oxyhydroxide deposits and cemented breccias (Figs. 5, 8, 9A). Fine laminations in the pyrite-marcasite (e.g., Fig. 9C) and barite-anhydrite crusts (Fig. 8G) suggest that they may have formed as a result of pulsating

hydrothermal discharge, similar to that observed in seafloor hydrothermal vents affected by tidal forcing. Less common are chimneys signifying focused venting, with the Twin Towers chimney complex the only one of any significance (Fig. 9E-H). Some (unsampled) mound structures were noted in the area (Fig. 8H), and while we believe they most likely represent the base of chimney structures such as the Twin Towers, they could represent accumulations of crusts. Plume-derived R/Ra values of 7.20 ± 0.28 (1999) and 7.05 ± 0.10 (2011), and a vent fluid derived value of 6.9 ± 0.05 (2005) suggest a chronic style of venting for this system over at least 13 years.

Much of the mineralization at Clark is dominated by sulfates, especially barite (Figs. 8–10, 12). Sulfides other than pyrite-marcasite are minor, with lesser sphalerite and galena; geochemical analyses show very low Cu contents (Appendix 2A). In general, the trace element contents for Clark mineralized samples are similar to other barite-rich hydrothermal precipitates associated with arc volcanoes elsewhere (e.g., de Ronde et al., 2011; Hein et al., 2014; Peterson et al., 2014; Yeats et al., 2014). Gold is present in 28 of the 31 Clark samples analyzed, averaging 2.9, and 8.1 ppm for the fisherman barite-pyrite sample (Appendix 2A; Fig. 9B). This compares with average values for Au of 7.6 ppm for Brothers mineralized samples, where Cu-rich chimneys in particular can have zones containing up to 91.4 ppm Au (de Ronde et al., 2011). Mercury in the Clark samples averages 87 ppm compared to only 20 ppm for Brothers samples.

Sulfur isotope ratios for Clark sulfides and sulfates (Table 2) are typical for low-temperature hydrothermal deposits on the seafloor. Sulfate $\delta^{34}S$ values of around 21‰ indicate a largely seawater origin. Moreover, positive $\delta^{34}S$ values for the sulfides (Table 2) are in contrast to those from sites known to expel fluids enriched in magmatic gases, like those of the Cone site, Brothers volcano (de Ronde et al., 2011). There, negative $\delta^{34}S$ values for sulfur range to –11‰, while values for the sulfate natroalunite are shifted to more negative values from seawater. Mineralized breccia, stockwork, and the Au-rich Cu-dominant chimneys of the NW Caldera site at Brothers also have negative $\delta^{34}S$ values, to –5‰ (de Ronde et al., 2011). This suggests that the fluids reaching the seafloor at Clark are dominated by (modified) seawater solutions that do not contain a significant magmatic component, consistent with the fluid chemistry being affected by water/rock reactions.

High Au/base metal values for the Clark pyrite mineralized samples (Appendix 2) are similar to Au-rich anhydrite chimneys seen at Axial Seamount (Hannington et al., 1999) and are consistent with subseafloor boiling and deposition of base metals at depth. This would be coherent with the top of the NW cone being dominated by volcaniclastic material, ensuring that permeability in this part of the volcano is distributed and not focused like at the NW Caldera site of Brothers.

Evidence for protracted mineralization at Clark

We believe that where venting is diffuse at Clark, the ascending hydrothermal fluid, already rich in Ba and Ra from the host rock, has time to dissolve barite from older, subseafloor mineralization. Due to radioactive decay, barite in the subseafloor is relatively low in ^{226}Ra and there is virtually no ^{228}Ra. Hence, the addition of older Ba and Ra to the

discharging hydrothermal fluid will lower the ^{226}Ra/Ba and ^{228}Ra/^{226}Ra values for the barite precipitating on the seafloor. The proportion of old to new barite therefore determines the ^{228}Ra/^{226}Ra for recent mineralization and this can have a wide range of values as shown by our theoretical mixing line (Appendix 3). Thus, the ^{228}Ra/^{226}Ra dating method cannot be applied to all samples from Clark volcano, where much of the barite is of mixed age.

For example, sample PV634-9R/B, from a white, barite-rich vent discharging 206°C fluid (cf. Fig. 9E, F), is an instance of new mineralization that has a component of significantly older barite. Radiometric dating using ^{228}Th/^{228}Ra values give ages for the most recent mineralization of 1.29 ± 0.04 and 0.49 ± 0.02 years for the inner and outer zones of the chimney, respectively (Table 3). However, the ^{226}Ra/Ba values for these zones (13.4 ± 0.2 and 14.1 ± 0.1 Bq.g^{-1}) are low compared with the estimated initial value of 19.1 ± 0.4 Bq.g^{-1} (Appendix 1). From the decrease in ^{226}Ra/Ba values due to radioactive decay, the minimum age for the redeposited (i.e., originating in the subseafloor) barite is ~750 years. However, the age can be better estimated if the percentage of new barite in each sample is known. This can be calculated from the ^{228}Ra/Ba values (6.72 ± 1.13 and 8.71 ± 0.17 Bq.g^{-1}) once they have been decay corrected to the time of mineralization, using ages derived from ^{228}Th/^{228}Ra values. Because the component that is older barite has no ^{228}Ra, the adjusted ^{228}Ra/Ba values (i.e., 7.85 ± 0.15 and 9.24 ± 0.18 Bq.g^{-1}) are still lower than the initial value of 17.85 ± 0.33 Bq.g^{-1}. Thus, from the low ^{228}Ra/Ba values we estimate 44.0 and 51.8% of the barite in the inner and outer chimney zones, respectively, is very young with the remainder having been redeposited (Table 3). Then, using the percentages of new barite, the initial ^{226}Ra/Ba value of 19.1 ± 0.4 Bq.g^{-1}, and the ^{226}Ra/Ba values for the samples of 13.44 ± 0.15 and 14.11 ± 0.15 Bq.g^{-1}, respectively, we calculate ^{226}Ra/Ba values of 9.01 ± 0.47 and 8.76 ± 0.61 Bq.g^{-1} for the remobilized barite. This equates to an average age of 1,770 ± 100 years, assuming the barite has not been repeatedly dissolved and redeposited.

Having dated the older barite redeposited in recent mineralization at one active vent, we combined the data from several samples to determine an average age for barite redeposited in the same general area. Plotting ^{226}Ra/Ba versus ^{228}Ra/Ba for different Clark samples produces a mixing line for old and new barite (Appendix 3). The y-axis intercept gives the ^{226}Ra/Ba value for the older barite component and, by comparison with the ^{226}Ra/Ba value for 100% new barite, gives an age of 2,700 ± 300 years. Deviations from the mixing line shown in Appendix 3 exceed the 1σ errors due to counting statistics, which suggests that the older barite in the Clark samples is not all of the same age. Considering that the samples give indications of major hydrothermal events at 19,000 years ago, between 3,000 and 4,000 years ago, and possibly at 5,000 and 1,800 years ago (Table 3), some barite could easily have been repeatedly dissolved and coprecipitated with newly extracted Ba and Ra.

All the mineralized samples from Brothers volcano by comparison are relatively young and, except for two outliers, have consistent ^{226}Ra/Ba and ^{228}Ra/Ba values (de Ronde et al., 2005, 2011; Ditchburn et al., 2012). For example, although there is a suggestion of a small component (~6.5% on average)

of older barite in Lena chimney, this has minimal affect on the ages (see Appendix 3). Thus, in stark contrast to Clark, there is little evidence for significant amounts of reworked, older barite in chimneys being formed today at Brothers volcano. This in turn suggests that hydrothermal systems of varying age and duration occur along the Kermadec arc, and that the older ones, such as at Clark, could have a propensity to form larger massive sulfide deposits, albeit largely subseafloor.

Finally, in an earlier study Ditchburn et al. (2012) suggested that the excess ^{228}Ra (i.e., high ^{228}Ra/^{226}Ra values) in Brothers volcano mineralization originated from ^{232}Th in subducted sediment. In this scenario, any excess ^{228}Ra would have to pass through the volcano from its deep-seated origin in less than 35 years. However, the magma at arc volcanoes ascends so slowly that any excess ^{228}Ra (with respect to the parent ^{232}Th) will most likely have decayed completely by the time the lava erupts (Turner et al., 2004). With further insight provided by the Clark samples, we now believe the high ^{228}Ra/^{226}Ra values for Clark (and other arc volcano) mineralization can be more simply explained by hydrothermally altered rock supplying the excess ^{228}Ra (also mentioned in Ditchburn et al., 2012). This is consistent with the radiogenic and REE data mentioned above that suggests the hydrothermal fluid has interacted with a plagioclase-rich source rock.

Model of the Clark hydrothermal system

Regional gravity data suggest that Clark volcano has had a complicated history of formation, with its location due to a large-scale normal fault that has a significant throw of several kilometers (Fig. 14). This history includes an apparently older, more tectonized SE cone and a volcanically younger NW cone (Fig. 4A). High-resolution magnetic data over the NW cone is consistent with a complex history of edifice construction, with a buried magnetized circular structure (coincident with a gravity low) occurring ~350 m below the summit believed to represent the margins of a caldera that has since been filled by further volcanic activity on the seafloor.

In addition, magnetic lows, or burn holes, appear in the geophysical data covering the NW cone, which we ascribe to hydrothermal upflow zones where magnetite has been altered to pyrite, effectively reducing the magnetization of the host rock. This effect has been described for Brothers and Rumble III volcanoes of the Kermadec arc (Caratori Tontini et al., 2012, 2013), and Palinuro and Marsili volcanoes of the Aeolian arc (Caratori Tontini et al., 2014). The burn holes all occur inside the walls of the postulated caldera. However, all the venting today occurs near the northern peak, along the ridge spur, or in the head scarps of sector collapses on either side of the spur (i.e., in the center of the cone), yet the burn holes to the north and west of the summit are not associated with present-day venting (Fig. 7). Thus, we believe the hydrothermal system was initiated soon after caldera formation and has then continued through the cone building stage (Fig. 17).

Having a two-stage evolution of the hydrothermal system at the NW cone of Clark has important connotations for the formation of buried massive sulfide deposits. That is, if we assume at least 200-m-high caldera walls (the caldera walls at the larger Brothers caldera are 290–530 m high), then the hydrothermal fluids would have exited the seafloor at least 550 m deeper than they are today (Fig. 17), meaning fluid
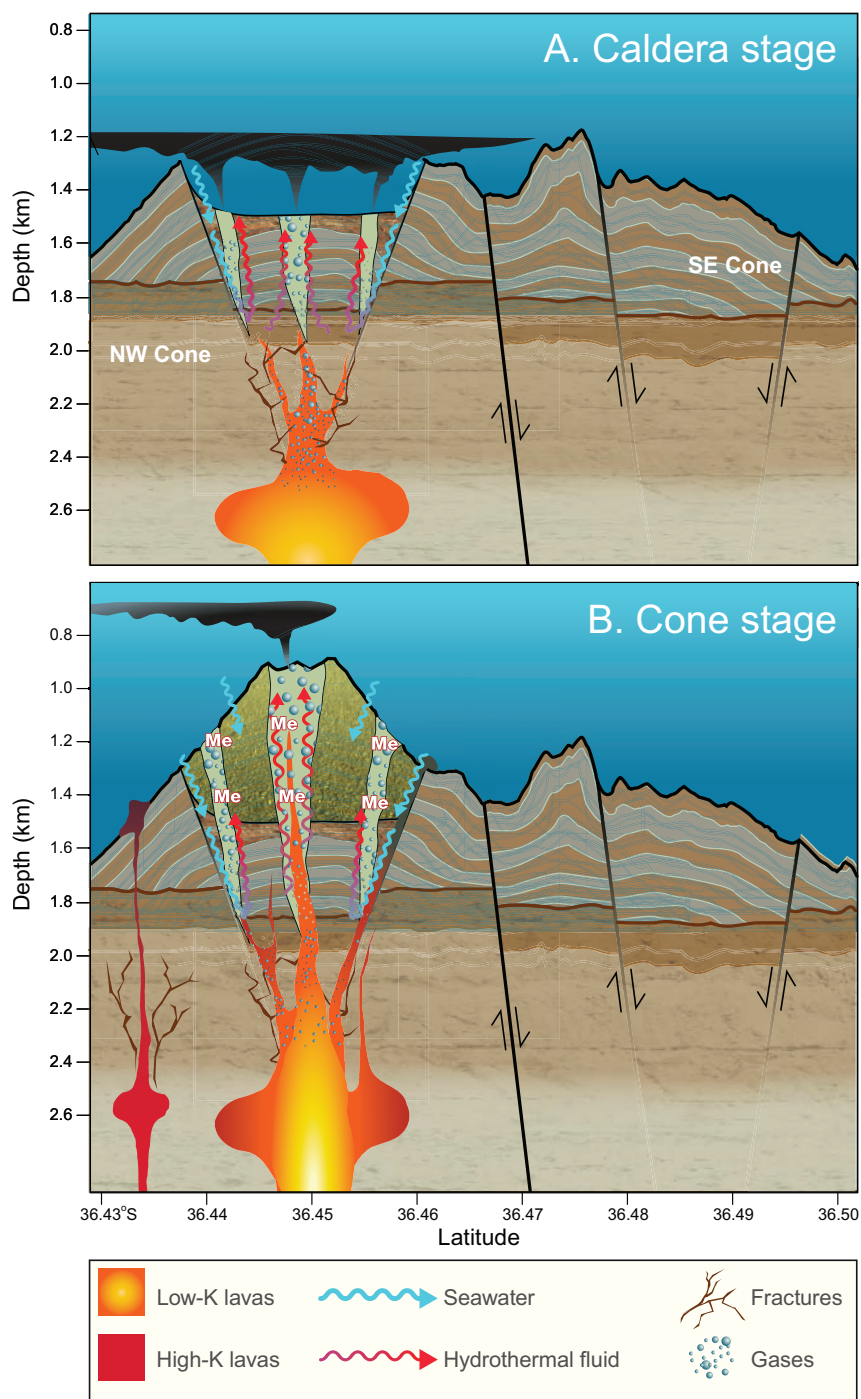
FIG. 17. Cartoon showing the transition from an initial caldera-forming event (A) to a cone-building event (B) at the NW cone edifice of Clark volcano. The heavily degraded summit of the SE cone, with its absence of a discernible summit crater and large-scale sector collapse, suggests that this cone is older than the NW cone, although we are uncertain of the absolute age of either cone. During the caldera stage of the NW cone, hydrothermal activity was most likely focused along caldera ring faults (cf. Brothers volcano), with recharge by seawater occupying similar faults. The cone stage represents further volcanic activity at the NW cone, with the caldera now filled by pyroclastics, lavas, and volcaniclastics. This implies that the top of the NW cone is most likely highly permeable, allowing deep penetration by seawater. Hydrothermal fluids could then boil (following the depth-to-boiling-point curve) and/or mix with ambient seawater several hundred meters subseafloor, enabling large quantities of metals to be deposited inside the cone, consistent with metal-poor fluids currently venting at the summit. Remobilization of metals such as Cu, deposited during the earlier (and deeper) caldera stage, would mean transportation to shallower depths. Gases depicted in the cartoon represent direct magmatic gas discharge (largely in the caldera stage) with the added effect of boiling (largely in the cone stage). High K lavas are considered late stage and are not associated with the low K, caldera-forming event, analogous to the evolution of Mount Taranaki volcano, onshore New Zealand (Zernack et al., 2012). Me = metals.

temperatures could have been hotter (~350°C for a seawater solution; Monecke et al., 2014), much like conditions today at Brothers (de Ronde et al., 2011). This in turn implies that mineralization formed at or below the seafloor, then, was more likely to contain Cu given the Brothers analogy and the propensity of Cu to be transported at higher temperatures (de Ronde et al., 2011, and references therein).

Permeability also plays an important role in the formation of massive sulfide deposits at arc volcanoes. For example, we know that permeability related to calderas is largely focused and governed by caldera ring faults (e.g., de Ronde et al., 2011; Barker et al., 2012; Embley et al., 2012; Gruen et al., 2012) whereas permeability related to cones is more distributed, or porous (e.g., Gruen et al., 2014; this work). Thus, hot, metal-pregnant fluids are more likely to rapidly ascend to the seafloor in calderas, whereas with cones the fluids can be expected to rise less quickly but interact extensively with rocks within the volcanic pile. Thus, any earlier precipitated mineralization associated with the now-extinct caldera stage of the NW cone could have been subjected to zone refining, or remobilization, by continuing hydrothermal activity related to the cone stage (Fig. 17). Moreover, a predominance of volcaniclastics comprising the cone would enhance widespread permeability, enabling ambient seawater to penetrate below the seafloor while promoting boiling of ascending hydrothermal fluids as the boiling-point-with-depth curve would effectively transcend the subseafloor, most likely by up to several hundred meters. Thus, hydrothermal fluids enriched in metals could preferentially deposit potential ore-grade mineralization between the older caldera floor and the cone summit.

The presence of magmatic fluid at Clark is ambiguous and certainly not as apparent as at Brothers volcano (de Ronde et al., 2005, 2011). Magmatic gas such as helium is obviously being expelled, although sulfur gases and CO_2 are not apparent in the concentrations seen at Brothers, and there is no sign of particularly acid fluids, or high sulfidation mineral assemblages occurring at Clark. This is either because the magma body beneath the NW cone has largely exsolved its gases or, more likely, boiling and mixing of the hydrothermal fluids with seawater within the pile of volcaniclastics has stripped both sulfur and metals from the parent fluid. If so, then high contents of Cu and Au commonly associated with magmatic fluids at Brothers (e.g., de Ronde et al., 2011; Berkenbosch et al., 2012) would be found in the inferred upflow zones within the cone (Fig. 17). This is consistent with the Pb isotope data, which suggests a magmatic source for this element.

A number of lines of evidence are consistent with both the remobilization of older mineralization and water/rock reactions taking place below the summit of the NW cone. For example, many of the chimneys and mineralized crusts found at the summit show good evidence for the incorporation of Ba derived from appreciably older barite (Table 3, Appendix 3). While the present-day chimneys all look to have formed within the past 20 years or so, they show evidence for numerous hydrothermal episodes during the past ~19,000 years (Table 3). Geochemical data show that the ultimate source of the vent fluid chemistry is dissolution of plagioclase from low K host rocks, possibly dissolved from old caldera material, with a significant addition of seawater. Combined, these data show that the NW cone hydrothermal system is long-lived,

has been witness to discreet episodes of activity, and has remobilized earlier mineralization.

In summary, a holistic approach to the study of the Clark hydrothermal system has revealed a two-stage process whereby a caldera-forming volcanic event preceded a later cone-building event. This ensured a protracted (at least 20,000-yr) history of hydrothermal activity and associated mineral deposition. The volcaniclastic units of the cone act as a large-scale filter, enabling hydrothermal fluids to boil and mix with seawater subseafloor, effectively removing the (largely base) metals in solution before they reach the seafloor. This has implications for recent estimates for the metal inventory of seafloor hydrothermal systems, especially those pertaining to arc hydrothermal systems (i.e., Hannington et al., 2011; Singer, 2013), which may be grossly underestimated.

Acknowledgments

REFERENCES

Baker, E.T., and Milburn, H.B., 1997, MAPR: A new instrument for hydrothermal plume mapping: RIDGE Events, Newsletter of the Ridge 2000 program (http://ridge2000.bio.psu.edu/science/contact.html), v. 8, p. 23–25.

Baker, E.T., Walker, S.L., Embley, R.W., and de Ronde, C.E.J., 2012, High-resolution hydrothermal mapping of Brothers caldera, Kermadec arc: Economic Geology, v. 107, p. 1583–1593.

Baker, J.A., Peate, D., Waight, T.E., and Meyzen, C., 2004, Pb isotopic analysis of standards and samples using a $^{207}Pb/^{204}Pb$ double spike and thallium to correct for mass bias with a double focusing MC-ICP-MS: Chemical Geology, v. 211, p. 275–303.

Barker, S., Wilson, C.J.N., Baker, J.A., Millet, M.-A., Rotella, M.D., Wright, I.C., and Wysoczanski, R.J., 2012, Geochemistry and petrogenesis of silicic magmas in the intra-oceanic Kermadec Arc: Journal of Petrology, v. 54, p. 351–391.

Berkenbosch, H.A., de Ronde, C.E.J., Gemmell, J.B., McNeill, A.W., and Goeman, K., 2012, Mineralogy and formation of black smoker chimneys from Brothers submarine volcano, Kermadec arc: Economic Geology, v. 107, p. 1613–1633.

Binns, R.A., 2014, Bikpela: A large siliceous chimney from the PACMANUS hydrothermal field, Manus basin, Papua New Guinea: ECONOMIC GEOLOGY, v. 109, p. 2243–2259.

Campbell, A.C., Palmer, M.R., Klinkhammer, G.P., Bowers, T.S., Edmond, J.M., Lawrence, J.R., Casey, J.F., Thompson, G., Humphris, S., Rona, P., and Karson, J.A., 1988, Chemistry of hot springs on the Mid-Atlantic Ridge: Nature, v. 335, p. 514–519.

Campbell, M.E., Rowland, J.V., Wright, I.C., and Smith, I.E.M., 2007, Oblique rifting along the central and southern Kermadec arc front: SW Pacific: Geochemistry Geophysics Geosystems, v. 8, doi:10.1029/2006GC001504.

Caratori Tontini, F., Graziano, F., Cocchi, L., Carmisciano, C., and Stefanelli, P., 2007, Determining the optimal Bouguer density for a gravity data set: Implications for the isostatic setting of the Mediterranean Sea: Geophysical Journal International, v. 169, p. 380–388.

Caratori Tontini, F., Cocchi, L., and Carmisciano, C., 2009, Rapid 3D forward model of potential field with application to the Palinuro Seamount (southern Tyrrhenian Sea, Italy): Journal of Geophysical Researches, v. 114, B02103, doi:10.1029/2008JB005907.

Caratori Tontini, F., Cocchi, L., Muccini, F., Carmisciano, C., Marani, M., Bonatti, E., Ligi, M., and Boschi, E., 2010, Potential-field modeling of collapse-prone submarine volcanoes in the southern Tyrrhenian Sea (Italy): Geophysical Research Letters, v. 37, L03305, doi:10.1029/2009GL041757.

Caratori Tontini, F., Davy, B., de Ronde, C.E.J., Embley, R.W., Leybourne, M., and Tivey, M.A., 2012, Crustal magnetization of Brothers volcano, New Zealand, measured by autonomous underwater vehicles: Geophysical expression of a submarine hydrothermal system: ECONOMIC GEOLOGY, v. 107, p. 1571–1581.

Caratori Tontini, F., de Ronde, C.E.J., Kinsey, J.C., Soule, A., Yoerger, D., and L. Cocchi, 2013, Geophysical modeling of collapse-prone zones at Rumble III seamount, southern Pacific Ocean, New Zealand: Geochemistry Geophysics Geosystems, v. 14, 4667–4680, doi:10.1002/ggge.20278.

Caratori Tontini, F., Bortoluzzi, G., Carmisciano, C., Cocchi, L., de Ronde, C.E.J., Ligi, M., and Muccini, F., 2014, Near-bottom magnetic signatures of submarine hydrothermal systems at Marsili and Palinuro volcanoes, southern Tyrrhenian Sea, Italy: ECONOMIC GEOLOGY, v. 109, p. 2119–2128.

Casanova, S.C., 2012, Morphometric analysis of the tectono-magmatic relationship governing the development of submarine volcanoes of the southern Kermadec arc: Unpublished B.Sc. Honors thesis, University of Sydney, 112 p.

Chu, M.-F., Wang, K.-L., Griffin, W.L., Chung, S.-L., O'Reilly, S.Y., Pearson, N.J., and Iizuka, Y., 2009, Apatite composition: Tracing petrogenetic processes in Transhimalayan granitoids: Journal of Petrology, v. 50, p. 1829–1855.

Craddock, P.R., Bach, W., Seewald, J.S., Rouxel, O.J., Reeves, E., and Tivey, M.K., 2010, Rare earth element abundances in hydrothermal fluids from the Manus basin, Papua New Guinea: Indicators of sub-seafloor hydrothermal processes in back-arc basins: Geochimica et Cosmochimica Acta, v. 74, p. 5494–5513.

Dekov, V.M., Kamenov, G.D., Abrasheva, M.D., Capaccioni, B., and Munnik, F., 2013, Mineralogical and geochemical investigation of seafloor massive sulfides from Panarea platform (Aeolian arc, Tyrrhenian Sea): Chemical Geology, v. 335, p. 136–148.

de Ronde, C.E.J., 2006, Mineralization associated with submarine volcanoes of the southern Kermadec arc, New Zealand: Australian Institute of Mining and Metallurgy Monograph 25, p. 333–338.

de Ronde, C.E.J., Faure, K., Bray, C.J., Chappell, D.A., and Wright, I.C., 2003, Hydrothermal fluids associated with seafloor mineralization at two southern Kermadec arc volcanoes, offshore New Zealand: Mineralium Deposita, v. 38, p. 217–233.

de Ronde, C.E.J., Hannington, M.D., Stoffers, P., Wright, I.C., Ditchburn, R.G., Reyes, A.G., Baker, E.T., Massoth, G.J., Lupton, J.E., Walker, S.L., Greene, R.R., Soong, C.W.R., Ishibashi, J., Lebon, G.T., Bray, C.J., and Resing, J.A., 2005, Evolution of a submarine magmatic-hydrothermal system: Brothers volcano, southern Kermadec arc, New Zealand: ECONOMIC GEOLOGY, v. 100, p. 1097–1133.

de Ronde, C.E.J., Baker, E.T., Massoth, G.J., Lupton, J.E., Wright, I.C., Sparks, R.J., Bannister, S.C., Reyners, M.E., Walker, S.L., Greene, R.R., Ishibashi, J., Faure, K., Resing, J.A., and Lebon, G.T., 2007, Submarine hydrothermal activity along the mid-Kermadec arc, New Zealand: Large-scale effects on venting: Geochemistry Geophysics Geosystems, v. 8, Q07007, doi:10.1029/2006GC001495.

de Ronde, C.E.J., Massoth, G.J., Butterfield, D.A., Christenson, B.W., Ishibashi, J., Ditchburn, R.G., Hannington, M.D., Brathwaite, R.L., Lupton,

J.E., Kamenetsky, V.S., Graham, I.J., Zellmer, G.F., Dziak, R.P., Embley, R.W., Dekov, V.M., Munnik, F., Lahr, J., Evans, L.J., and Takai, K., 2011, Submarine hydrothermal activity and gold-rich mineralization at Brothers volcano, Kermadec arc, New Zealand: Mineralium Deposita, v. 46, p. 541–584, DOI 10.1007/s00126-011-0345-8.

Ditchburn, R.G., de Ronde, C.E.J., and Barry, B.J., 2012, Radiometric dating of volcanic massive sulfides and associated iron oxide crusts with an emphasis on ²²⁶Ra/Ba and ²²⁸Ra/²²⁶Ra in volcanic and hydrothermal processes at intraoceanic arcs: ECONOMIC GEOLOGY, 107, p. 1635–1648.

Embley, R.W., de Ronde, C.E.J., Merle, S. G., Davy, B., and Caratoni Tontini, F., 2012, Detailed morphology and structure of an active submarine arc caldera: Brothers volcano, Kermadec arc: ECONOMIC GEOLOGY, v. 107, p. 1557–1570.

Finlay, C.C, Maus, S., Beggan, C.D., Bondar, T.N., Chambodut, A., Chernova, T.A., Chulliat, A., Golovkov, V.P., Hamilton, B., Hamoudi, M., Holme, R., Hulot, G., Kuang, W., Langlais, B., Lesur, V., Lowes, F.J., Lühr, H., Macmillan, S., Mandea, M., McLean, S., Manoj, C., Menvielle, M., Michaelis, I., Olsen, N., Rauberg, J., Rother, M., Sabaka, T.J., Tangborn, A., Tøffner-Clausen, L., Thébault, E., Thomson, A.W.P., Wardinski, I., Wei, Z., and Zvereva, T.I., 2010, International Geomagnetic Reference Field: The eleventh generation: Geophysical Journal International, v. 183, p. 1216–1230.

Fouquet, Y., and Marcoux, E., 1995, Lead isotope systematics in Pacific hydrothermal sulfide deposits: Journal of Geophysical Research, v. 100, p. 6025–6040.

Gamble, J.A., Woodhead, J., Wright, I.C., and Smith, I.E.M., 1996, Basalt and sediment geochemistry and magma petrogenesis in a transect from oceanic island arc to rifted continental margin arc: The Kermadec-Hikurangi margin, SW Pacific: Journal of Petrology, v. 37, p. 1523–1546.

Gamble, J.A., Christie, R.H.K., Wright, I.C., and Wysoczanski, R.J., 1997, Primitive K-rich magmas from Clark volcano, southern Kermadec Arc: A paradox in the K-depth relationship: Canadian Mineralogist, v. 35, p. 275–290.

Gruen, G., Weis, P., Driesner, T., de Ronde, C.E.J., and Heinrich, C.A., 2012, Fluid-flow patterns at Brothers volcano, southern Kermadec arc: Insights from geologically constrained numerical simulations: ECONOMIC GEOLOGY, v. 107, p. 1595–1611.

Gruen, G., Weis, P., Driesner, T., Heinrich, C.A., and de Ronde, C.E.J., 2014, Hydrodynamic modeling of magmatic-hydrothermal activity at submarine arc volcanoes with implications for ore deposit formation: Earth and Planetary Science Letters, v. 404, p. 307–318.

Haase, K.M., Worthington, T.J., Stoffers, P., Garbe-Schoenberg, D., and Wright, I., 2002, Mantle dynamics, element recycling, and magma genesis beneath the Kermadec arc-Havre trough: Geochemistry Geophysics Geosystems, v. 3, doi:10.1029/2002GC000335.

Hannington, M.D., Poulsen, K.H., Thompson, J.F.H., and Sillitoe, R.H., 1999, Volcanogenic gold in the massive sulfide environment: Reviews in Economic Geology, v. 8, p. 319–350.

Hannington, M.D., Jamieson, J., Monecke, T., Petersen, S., and Beaulieu, S., 2011, The abundance of seafloor massive sulfide deposits: Geology, v. 39, p. 1155–1158.

Hein, J.R., de Ronde, C.E.J., Koski, R.A., Ditchburn, R.G., Mizell, K., Tamura, Y., Stern, RJ., Conrad, T.A., Ishizuka, O., and Leybourne, M.I., 2014, Layered hydrothermal barite-sulfide bound field, East Diamante caldera, Mariana volcanic arc: ECONOMIC GEOLOGY, v. 109, p. 2179–2206.

Kamenov, G.D., Perfit, M.R., Jonasson, I.R., and Mueller, P.A., 2005, High-precision Pb isotope measurements reveal magma recharge as a mechanism for ore deposit formation: Examples from Lihir Island and Conical seamount, Papua New Guinea: Chemical Geology, v. 219, p. 131–148.

Kamenov, G.D., Perfit, M.R., Mueller, P.A., and Jonasson, I.R., 2008, Controls on magmatism in an island arc environment: Study of lavas and sub-arc xenoliths from the Tabar-Lihir-Tanga-Feni island chain, Papua New Guinea: Contributions to Mineralogy and Petrology, v. 155, p. 635–656.

Klinkhammer, G.P., Elderfield, H., Edmond, J.M., and Mitra, A., 1994, Geochemical implications of rare earth element patterns in hydrothermal fluids from mid-ocean ridges: Geochimica et Cosmochimica Acta, v. 58, p. 5105–5113.

Leybourne, M.I., de Ronde, C.E.J., Wysoczanski, R.J., Walker, S.L., Timm, C., Gibson, H.L., Layton-Matthews, D., Baker, E.T., Clark, M.R., Caratori-Tontini, F., Faure, K., Lupton, J.E., Fornari, D.J., Soule, S.A., and Massoth, G.J., 2012a, Geology, hydrothermal activity, and seafloor massive sulfide mineralization at the Rumble II West mafic caldera: ECONOMIC GEOLOGY, v. 107, p. 1649–1668.

Leybourne, M.I., Schwarz-Schampera, U., de Ronde, C.E.J., Baker, E.T., Faure, K., Walker, S.L., Butterfield, D.A., Resing, J., Lupton, J.E., Hannington, M.D., Gibson, H.L., Massoth, G.J., Embley, R.W., Chadwick, W.W., Jr., Clark, M.R., Timm, C., Graham, I.J., and Wright, I.C., 2012b, Submarine magmatic-hydrothermal systems at the Monowai volcanic center, Kermadec arc: Economic Geology, v. 107, p. 1669–1694.

Ling, H.F., Burton, K.F., O'Nions, R.K., Kamber, B.S., von Blanckenburg, F., Gibb, A.J., and Hein, J.R., 1997, Evolution of Nd and Pb isotopes in Central Pacific seawater from ferromaganese crusts: Earth and Planetary Science Letters, v. 146, p. 1–12.

Luais, B., Telouk, P., and Albarède, F., 1997, Precise and accurate neodymium isotopic measurements by plasma-source mass spectrometry: Geochimica et Cosmochimica Acta, v. 61, p. 4847–4854.

Merle, S., Embley, B., and Chadwick, B., 2006, New Zealand American Submarine Ring of Fire 2005 (NZASRoF '05)—Kermadec arc submarine volcanoes, R/V *Ka-imikai-o-Kanaloa*: Cruises KOK05-05 and KOK05-06, 125 p.

Meyzen, C.M., Blichert-Toft, J., Ludden, J.N., Humler, E., Mevel, C., and Albarede, F., 2007, Isotopic portrayal of the Earth's upper mantle flow field: Nature, v. 447, p. 1069–1074.

McCoy-West, A.J., Baker, J.A., Faure, K. and Wysoczanski, R.J., 2010, Petrogenesis and origins of Mid-Cretaceous continental intraplate volcanism in Marlborough, New Zealand: Implications for the long-lived HIMU magmatic mega-province of the SW Pacific: Journal of Petrology, v. 51, p. 2003–2045.

Michard, A., Albarede, F., Michard, G., Minster, J.F., and Charlou, J.L., 1983, Rare-earth elements and uranium in high-temperature solutions from East Pacific Rise hydrothermal vent field (13°N): Nature, v. 303, p. 795–797.

Monecke, T., Petersen, S., and Hannington, M.D., 2014, Constraints on water depth of massive sulfide formation: Evidence from modern seafloor hydrothermal systems in arc-related settings: Economic Geology, v. 109, p. 2079–2101.

Ohmoto, H., and Lasaga, A.C., 1982, Kinetics of reactions between aqueous sulfates and sulfides in hydrothermal systems: Geochemica et Cosmochimica Acta, v. 46, p. 1727–1745.

Ohmoto, H., and Rye, R.O., 1979, Isotopes of sulfur and carbon, *in* Barnes, H.L., ed., Geochemistry of hydrothermal ore deposits, 2nd ed.: New York, Wiley-Interscience, p. 509–567.

Paris, G., Sessions, A.L., Subhas, A.V., and Adkins, J.F., 2013. MC-ICP-MS measurement of δ^{34}S and Δ^{33}S in small amounts of dissolved sulfate: Chemical Geology, v. 345, p. 50–61.

Petersen, S., Monecke, T., Westhues, A., Hannington, M.D., Gemmell, J.B., Sharpe, R., Peters, M., Strauss, H., Lackschewitz, K., Augustin, N., Gibson, H., and Kleeberg, R., 2014, Drilling shallow-water massive sulfides at the Palinuro volcanic complex, Aeolian island arc, Italy: Economic Geology, v. 109, p. 2129–2157.

Robinson, B.W., 1977, Isotopic equilbria in hydrothermal barites: New Zealand Department of Scientific and Industrial Research Bulletin, v. 218, p. 51–56.

Saunders, K.E., Baker, J.A., and Wysoczanski, R.J., 2010, Microanalysis of large volume silicic magma in continental and oceanic arcs: Melt inclusions in Taupo volcanic zone and Kermadec arc rocks, South West Pacific: Journal of Volcanology and Geothermal Research, v. 190, p. 203–218.

Schmidt, K., Garbe-Schönberg, D., Bau, M., and Koschinsky, A., 2010, Rare earth element distribution in >400°C hot hydrothermal fluids from 5°S, MAR: The role of anhydrite in controlling highly variable distribution patterns: Geochimica et Cosmochimica Acta, v. 74, p. 4058–4077.

Seal, R.R., II, Alpers, C.N., and Rye, R.O., 2000, Stable isotopes systematics of sulfate minerals: Reviews in Mineralogy and Geochemistry, v. 40, p. 541–602.

Singer, Donald A., 2013, Base and precious metal resources in seafloor massive sulfide deposits: Ore Geology Reviews, doi: 10.1016/j.oregeorev.2013.11.008

Sun, S.-S., and McDonough, W.F., 1989, Chemical and isotopic systematics of oceanic basalts: Implications for mantle composition and processes: Geological Society of London Special Publications 42, p. 313–345.

Tatsumi, Y., Takahashi, T., Hirahira Y., Chang, Q., Miyazaki, T., Kimura, J.-I., Ban, M., and Sakayori A., 2008, New insights into andesite genesis: The role of mantle-derived calc-alkalic and crust-derived tholeiitic melts in magma differentiation beneath Zao volcano, NE Japan: Journal of Petrology, v. 49, p. 1971–2008.

Tivey, M.A., Schouten, H., and Kleinrock, M.C., 2003, A near-bottom magnetic survey of the Mid-Atlantic Ridge axis at 26 N: Implications for the tectonic evolution of the TAG segment: Journal of Geophysical Research, v. 108, p. 2277–2283.

Todd, E., Gill, J.B., Wysoczanski, R.J., Handler, M.R., Wright, I.C., and Gamble, J.A., 2010, Sources of constructional cross-chain volcanism in the southern Havre trough: New insights from the HFSE and REE concentration and isotope systematics: Geochemistry Geophysics Geosystems, v. 11, doi:10.1029/2009GC002888.

Todd, E., Gill, J.B., Wysoczanski, R.J., Hergt, J., Wright, I.C, Leybourne, M.I., and Mortimer, N., 2011, Hf isotopic evidence for small-scale heterogeneity in the mode of mantle wedge enrichment: Southern Havre trough and south Fiji basin back-arcs. Geochemistry Geophysics Geosystems, v. 12, doi:10.1029/2011GC003683.

Turner, S., Hawkesworth, C., Rogers, N., Bartlett, J., Worthington, T., Hergt, J., Pearce, J., and Smith, I., 1997, ^{238}U-^{230}Th disequilibria, magma petrogenesis, and flux rates beneath the depleted Tonga-Kermadec island arc: Geochimica et Cosmochimica Acta, v. 61, p. 4855–4884.

Turner, S., Black, S., and Berlo, K., 2004, ^{210}Pb-^{226}Ra and ^{228}Ra-^{232}Th systematics in young arc lavas: Implications for magma degassing and ascent rates: Earth and Planetary Science Letters, v. 227, p. 1–16.

Waight, T.E., Baker, J.A., and Peate, D., 2002, Sr isotope ratio measurements by double-focusing MC-ICPMS: Techniques, observations and pitfalls: International Journal of Mass Spectrometry, v. 221, p. 229–244.

Wright, I.C., Stoffers, P., Hannington, M., de Ronde, C.E.J., Herzig, P., Smith, I.E.M., and Browne, P.R.L., 2002, Towed-camera investigations of shallow-intermediate water-depth submarine basaltic stratovolcanoes of the southern Kermadec arc: Marine Geology, v. 185, p. 207–218.

Wysoczanski, R.J., Handler, M.R., Schipper, C.I., Leybourne, M.I., Creech, J., Rotella, M.D., Nichols, A.R.L., Wilson, C.J.N., and Stewart, R.B., 2012, The tectonomagmatic source of ore metals and volatile elements in the southern Kermadec arc: Economic Geology, v. 107, p. 1539–1556.

Yeats, C.J., Parr, J.M., Binns, R.A., Gemmell, B., and Scott, S.D., 2014, The SuSu Knolls hydrothermal field, eastern Manus basin, Papua New Guinea: An actively forming submarine high sulfidation copper-gold system: Economic Geology, v.109, p. 2207–2226.

Zernack, A.V., Price, R.C., Smith, I.E.M., Cronin, S. J. and Steward, R.B., 2012, Temporal evolution of a high-K andesitic magmatic system: Taranaki volcano, New Zealand: Journal of Petrology, v. 53, p. 325–363.

APPENDIX 1

Methods

Geophysics

Magnetic data were collected over Clark volcano using a Marine Magnetics Seaspy magnetometer towed 300 m behind the ship's stern to reduce the effects of magnetic noise. The data were processed for heading and lag errors, and the anomaly field was obtained by subtracting the 2011 International Geomagnetic Reference Field from the observed field (Finlay et al., 2010). The equivalent magnetization map was then obtained by inverting the magnetic anomalies (e.g., Caratori Tontini et al., 2012), using as an upper boundary the bathymetry and a constant bottom depth horizon of 2,500 m for the lower boundary, which marks the average depth of the seafloor surrounding Clark volcano (Fig. 1B).

High-resolution magnetic data were collected over the NW cone at Clark using a 3-axis Honeywell HMR2300 smart digital magnetometer aboard *Sentry*. The raw vector data were transformed into a total-intensity field and corrected for the magnetic noise generated by the AUV. This calibration is obtained by fitting the variation of the magnetic field while the AUV spins during its descent to the seafloor (Tivey et al., 2003; Caratori Tontini et al., 2012). These data were then corrected using the standard procedures described above for the surface magnetic data to obtain the magnetic anomaly grid. The equivalent magnetization map (Fig. 4C) was obtained by inversion of the magnetic anomaly grid (Caratori Tontini et al., 2012), using a layer enclosed by the seafloor (bathymetry) on its upper surface, with a constant thickness of 500 m.

Gravity data were collected using a Lacoste and Romberg dynamic gravity meter upgraded with a ZLS Ultrasys control system. Relative gravity was tied to an absolute station in Auckland harbor before and after the cruise to check for meter drift (<3 mGal/month). The drift-corrected data then were corrected for Eotvos effects and processed with a 120-sec Butterworth low-pass filter along the survey lines. The complete Bouguer correction was computed using a reference density of 2.4 g/cm^3. This is an optimal value arising from an analysis of the correlation between the gravity anomaly and the bathymetry (cf. Caratori Tontini et al., 2007).

Hydrothermal plumes

The distribution of seafloor hydrothermal activity at Clark has been determined using a variety of techniques. Initially, we employed the towed camera *OFOS* (Ocean Floor Observation System) equipped with MAPRs (Miniature Autonomous Plume Recorders; Baker and Milburn, 1997) to map a limited, near-bottom area on the NW Cone during the 1998 R/V *Sonne* cruise (Figs. 4–6; Table 1). Subsequently, during the 1999 NZAPLUME (New Zealand American PLUme Mapping Expedition), 2002 NZAPLUME II, and the 2011 NZASMS cruises, we deployed a combination CTDO/rosette package with discreet water sampling capability to determine the regional extent of hydrothermal emissions, by mapping plumes throughout the water column.

High-resolution plume mapping was achieved by attaching a single MAPR mounted on the stern of *Sentry*, which was set to sample at 5-s intervals. Shown in Figure 7 are values for dNTU, which is the anomaly above background (minimum mid-water column value), and oxidation-reduction potential (ORP) anomalies, which are the decrease in voltage from the value prior to when the decrease began, i.e., the signal is a relative change. Also, plots of dE/dt show the rate of change in the ORP, with E being the measured potential. Here, we present dE/dt for decreasing E, indicating the presence of reduced chemical species (e.g., Fe(II), H_2) and hence a measure of "young" hydrothermal plumes.

Mineralogy

Secondary electron images and energy dispersive X-ray spectra were obtained on small (~1 × 1 cm) subsamples from the Twin Towers chimney and the "fisherman" chimney, dried at a temperature of ~20°C, then mounted on aluminum stubs using carbon tape and coated with C using a LYRA (Tescan) focused ion beam equipped scanning electron microscope (SEM) at the University of Sofia, and a Cambridge S360 SEM at the Geological Survey of Canada. Operating conditions of the SEMs were 10 to 20 KeV, 12 nA, electron beam diameter = 2 μm at Sofia University and 20 KeV for the Cambridge S360 SEM at the Geological Survey of Canada.

Microprobe analyses of pyrite and clay minerals were obtained on carbon-coated polished thin sections of representative samples using a Cameca Camebax MBX electron microprobe equipped with wavelength dispersive spectrometers at the Geological Survey of Canada. Analytical conditions were 15-kV accelerating voltage with a 20- to 30-nA beam current, variable counting times of 10 to 20 s, and a beam diameter of ~5 μm. Analytical conditions for the clay minerals were varied depending on grain size and the degree of crystallinity of the clay minerals. Low and variable totals (not shown) are due to the water content of the clays, which was not analyzed. This does not affect classification of the clays, which is based on their major cations.

Particle induced X-ray emission (PIXE) analysis was performed to generate element maps from polished thin sections, using a 3-MeV H$^+$ beam from a 3-MV Tandetron accelerator at the Institute of Ion Beam Physics and Materials Research, Dresden-Rossendorf, Germany. The beam was focused to about 5 μm^2 and scanned areas ≤1 mm^2 over the various samples. A representative sample of a barite- and anhydrite-rich chimney recovered from the base of the accelerator is shown in Figure 12 (i.e., PV623-11R).

Stable isotopes

Sulfur and oxygen isotope analyses were performed at the National Isotope Center at GNS Science, Lower Hutt, and the University of Ottawa Hatch Laboratory, with the results given in Table 4. The δ^{34}S values are normalized using IAEA-S-1 = 0.0 ± 0.2‰ and are reported relative to V-CDT; they have a precision and accuracy of ±0.2‰. The δ^{18}O values are normalized using IAEA-SO-5 = 11.7 ± 0.2‰ and are reported relative to V-SMOW; they have a precision and accuracy of ±0.3‰.

Radiometric ages

The radiometric dating techniques used to date the Clark samples involve ^{228}Th, ^{228}Ra, and ^{226}Ra with half-lives of 1.91,

5.75, and 1,600 years, respectively (see Ditchburn et al., 2012, for details). For the Clark hydrothermal site, the isotope ratios at the time of mineralization, i.e., the initial ratios needed for dating older samples, were measured from recently formed chimneys that contained minimal redeposited, or older barite (see text).

We determined an initial ^{226}Ra/Ba value of 19.1 ± 0.4 Bq.g^{-1} by averaging the three highest values, 18.7 ± 0.3, 19.5 ± 0.3, and 19.2 ± 0.6 Bq.g^{-1} measured in samples PV623-8R, PV634-8R, and 74DR12, respectively (Table 3). Similarly, we determined an initial ^{228}Ra/^{226}Ra value (activity ratio) of 1.08 ± 0.03 Bq.Bq^{-1} estimated from the two highest values of 1.01 ± 0.04 and 1.04 ± 0.03 Bq.Bq^{-1} (again measured in samples PV623-8R and PV634-8R). These values were each decay corrected to time of mineralization, using ages derived from ^{228}Th/^{228}Ra values, and then averaged. Using a similar approach, an initial ^{228}Ra/Ba value of 17.85 ± 0.33 Bq.g^{-1} was derived from the highest values of 17.70 ± 0.50 and 18.01 ± 0.42 Bq.g^{-1} measured in the same two samples.

Sr, Nd, and Pb isotopes and trace element analyses

New Sr-Nd-Pb isotope data are presented in this study on six chimney sulfate (anhydrite, gypsum, and barite) and sulfide (pyrite and marcasite) samples, on three low K basaltic andesites and one high K basalt, all recovered from the NW Cone of Clark volcano (Table 4).

Strontium, Nd, and Pb isotope analyses were determined at the Department of Geological Sciences, University of Florida, and Victoria University of Wellington (VUW). At the University of Florida, all reagents used for trace element and isotope analyses were Optima-grade and sample preparation was done in a clean lab environment. Trace element analyses for the rock samples, including the REE, were performed on an Element2 HR-ICP-MS in medium resolution with Re and Rh used as internal standards. Quantification of results was done by external calibration using gravimetrically prepared ICP-MS standards (QCD Analysts, www.qcdanalysts.com). Whole-rock samples P74517 and P72932 were leached with 2N HCl to remove any effects of alteration by seawater before preparation for isotope analyses. Sr, Nd, and Pb were separated from the sample matrix using standard chromatographic methods and the isotopic compositions were determined on an "Nu-Plasma" MC-ICP-MS. Further details on the methods used are described in Kamenov et al. (2008).

Strontium, Nd, and Pb isotope analyses for Clark whole-rock samples C3 and C6 were done at VUW. Analytical procedures are modified from those described in Waight et al. (2002), Luais et al. (1997), and McCoy-West et al. (2010). Fresh rock chips were cleaned by repeated boiling and rinsing in double-distilled water to remove salt contamination, before being powdered. The powders were then leached in warm 6M HCl for one hour and rinsed repeatedly in >18.2MΩ water before conventional acid digestion using HF-HNO$_3$. Sr was separated using Sr-Spec Eichrom resin, and Nd using cation exchange and Ln-spec Eichrom resins. Lead was separated using conventional HBr-HCl based anion exchange chemistry. The reported ^{87}Sr/^{86}Sr values are relative to NBS 987 ^{87}Sr/^{86}Sr = 0.71025 (±0.00003, 2σ); Nd isotope compositions are relative to JNdi-1 ^{143}Nd/^{144}Nd = 0.512103 (±0.000018, 2σ; U of F; adjusted to a corresponding La Jolla ^{143}Nd/^{144}Nd value of 0.51186) and to Alfa Aesar Nd standard ^{143}Nd/^{144}Nd = 0.512260 (±0.000007, 2σ; VUW; corresponding to a La Jolla value of 0.51186). The Pb isotopic data are relative to NBS 981 = ^{206}Pb/^{204}Pb = 16.9416 (±0.004, 2σ), ^{207}Pb/^{204}Pb = 15.500 (±0.003, 2σ), and ^{208}Pb/^{204}Pb = 36.7262 (±0.009, 2σ). Lead isotope ratios for samples C3 and C6 were measured using SRM 981 for standard-sample bracketing to correct for instrumental mass bias (Baker et al., 2004).

APPENDIX 2A. Geochemistry

Type	Barite			Barite-pyrite							Barite-Mn	Barite-		
Sample no.	Clark-4B	P5-634-3R	P5-634-9R	Clark-4A	Clark-4B-1	Clark-4B-2	SO135-74DR 12-1	SO135-74DR 12-2	SO135-74DR 12-3	SO135-74DR 12-4	SO135-74DR8	Clark-2A	Clark-2B	Clark-3B
BaO (wt %)	60.3	60.18	58.03	41.6	35.4	13.4	39.8	12.7	16.1	24.5	39.4	23.1	33.5	24.9
CaO	<1.0	0.19	0.23	0.13	0.17	<2.0	0.19	2.74	2.13	0.15	0.3	22.8	13.5	20.9
SiO_2		0.12	0.05	0.5	1.3	--	3.0	1.2	7.0	3.6	3.8	1.7	1.3	1.1
Fe_2O_3 (Total)	0.77	0.22	0.37	16.9	22.7	54.5	11.7	38.4	35.5	29.6	0.39	1.11	2.19	1.57
TiO_2	--	<0.001	<0.001	<0.02	<0.02	--	<0.02	<0.02	<0.02	<0.02	<0.02	<0.02	<0.02	<0.02
Al_2O_3	--	<0.01	<0.01	<0.2	<0.2	--	<0.2	<0.2	0.2	<0.2	0.2	0.4	0.2	<0.2
MnO	--	<0.001	<0.001	0.02	0.02	--	0.02	0.01	0.01	0.02	3.56	<0.01	0.01	<0.01
MgO	--	<0.01	<0.01	<0.04	<0.04	--	<0.04	<0.04	<0.04	<0.04	0.31	0.18	0.06	0.07
Na_2O	0.42	0.04	0.05	0.04	0.1	0.03	0.04	0.04	0.03	0.04	0.18	0.24	0.13	0.34
K_2O	--	0.06	<0.01	<0.05	<0.05	--	<0.05	<0.05	<0.05	<0.05	0.08	0.06	<0.05	<0.05
CO_2 (Total)	--	0.07	0.07	0.1	--	--	0.1	0.1	0.2	0.1	0.1	0.2	0.1	0.2
P_2O_5	--	<0.01	<0.01	<0.01	0.01	--	<0.01	<0.01	<0.01	<0.01	0.03	0.01	<0.01	0.01
ST	--	15.2	15.2	24.9	27.2	--	19.7	36.4	33.8	30.6	13.1	19.6	18.6	20.2
LOI	--	0.6	0.7	9.1	11.8	--	6.4	23.3	20.9	17	1.5	2	3.1	1.6
Sr (ppm)	14,800	>10,000	>10,000	11,200	11,600	4,700	4,210	568	1,970	3,080	7,730	5,120	8,730	5,070
Rb	--	<2	<2	0.27	0.2	--	0.23	0.23	0.78	0.14	0.77	1.8	1	0.8
Cs	<1	<0.5	<0.5	0.12	0.07	<1	0.15	0.08	0.18	0.08	0.08	0.14	0.07	0.1
Be	--	<1	<1	<0.5	<0.5	--	<0.5	<0.5	<0.5	<0.5	<0.5	<0.5	<0.5	<0.5
Br	26.7	<0.5	<0.5	<0.5	8.9	<2	<0.5	<0.5	<0.5	<0.5	2.2	8.1	8.2	19.1
Cr	<5	<5	<5	<5	10	<5	15	20	15	16	10	<5	<5	<5
V	--	<5	<5	<5	<5	--	<5	<5	<5	<5	7	8	5	<5
Sc	<0.1	<0.1	<0.1	<0.5	<0.5	0.2	<0.5	<0.5	0.5	<0.5	<0.5	0.7	<0.5	<0.5
U	<0.5	<0.1	<0.1	0.29	0.25	<0.5	0.13	0.05	0.31	0.1	0.15	1.3	0.71	0.44
Th	<0.2	<0.1	<0.1	<0.02	<0.02	<0.2	<0.02	<0.02	<0.02	<0.02	<0.02	0.03	0.03	<0.02
Nb	--	<1	<1	0.08	0.11	--	<0.05	0.08	0.07	<0.05	<0.05	0.17	0.08	0.15
Zr	--	<4	8	<0.5	<0.5	--	100	200	180	244	18	4.2	<0.5	0.5
Y	--	<2	<2	0.08	0.09	--	0.04	0.07	0.1	0.03	0.84	0.52	0.36	0.52
Hf	<1	0.7	1.3	<0.05	<0.05	<1	2	4.2	3.7	5	0.32	0.1	<0.05	<0.05
Ta	<0.5	0.7	1.6	0.12	0.13	<0.5	<0.05	<0.05	<0.05	<0.05	<0.05	0.14	0.17	0.25
W	<1	<1	<1	40	52	<1	<1	<1	<1	<1	<1	29	49	71
As	89	28.7	27.8	2,590	3,250	1,080	1,420	7,030	5,920	7,430	11.3	83.9	147	115
Sb	5.5	35.5	26.8	88.2	86.6	219	57	110	100	93	4.1	10.7	24.7	16.9
Hg	17	70	113	1170	130	66	180	54	30	130	19	18	63	38
Cu	--	156	22	79	100	--	32	198	264	112	38	82	63	58
Zn	77	1,440	157	250	170	72	131	40	342	96	76	960	640	450
Pb	--	203	15	450	490	--	271	198	653	484	51	380	470	170
Ag	9	100	54.9	160	190	350	93	203	158	202	4.3	57	120	77
Au (ppb)	201	1,740	251	4,840	5,750	15,100	3,420	10,100	7,490	10,300	231	1,690	2,550	1,760
Bi (ppm)	--	<0.4	<0.4	<0.2	<0.2	--	<0.2	<0.2	<0.2	<0.2	<0.2	<0.2	<0.2	<0.2
Cd	--	13.2	0.6	0.5	0.5	--	0.3	<0.2	1.2	0.4	0.5	3.6	2.5	1.8
Ga	--	4	1	1.1	0.7	--	0.6	<0.1	1.4	0.4	5.5	2.8	1.7	1.3
Ge		<1	<1											
Tl	--	<0.1	<0.1	92	61	--	115	20	8.5	62	2.3	4.6	24	23
In	--	<0.2	<0.2	<0.05	<0.05	--	<0.05	<0.05	<0.05	<0.05	<0.05	<0.05	<0.05	<0.05
Sn	--	<1	<1	<0.5	0.6	--	<0.5	0.7	<0.5	1	<0.5	1.8	<0.5	0.7
Co	1	<1	<1	14	9	24	<5	6	16	<5	34	13	21	16
Se	<3	<3	<3	<3	<3	<3	<3	<3	<3	<3	13	<3	<3	4
Te	--	--	--	<0.2	<0.2	--	<0.2	<0.2	<0.2	<0.2	<0.2	<0.2	<0.2	<0.2
Mo	<3	9	3	3.1	5.2	<4	1.8	1.1	1.6	3.3	84	1	1.1	1
Ni	<30	<1	<1	11	<10	<50	<10	18	31	10	36	<10	<10	<10
La	4.8	1.5	1.2	1	1.1	5.7						0.4	1.4	0.2
Ce		1.5	1.2	1.5	1.6							0.8	2	0.5
Pr		0.06	<0.05	0.15	0.16							0.1	0.19	0.1
Nd		0.2	0.2	0.5	0.5							0.4	0.7	0.6
Sm		<0.1	<0.1	0.02	0.03							0.08	0.08	0.16
Eu		<0.05	<0.05	0.07	0.08							0.1	0.1	0.11
Gd		<0.1	<0.1	<0.02	<0.02							0.09	0.06	0.15
Tb		<0.1	0.2	<0.02	<0.02							0.02	<0.02	0.02
Dy		<0.1	<0.1	<0.02	<0.02							0.09	0.05	0.1
Ho		<0.1	<0.1	<0.02	<0.02							0.02	<0.02	0.02
Er		<0.1	<0.1	<0.02	<0.02							0.05	0.03	0.03
Tm		<0.05	<0.05	<0.02	<0.02							<0.02	<0.02	<0.02
Yb		<0.1	<0.1	<0.02	<0.02							0.05	0.02	0.02
Lu		<0.04	<0.04	<0.02	<0.02							<0.02	<0.02	<0.02

Notes: Analyzed by ICP-MS and ICP-ES at the Geological Survey of Canada laboratories; fusion followed by multi-acid dissolution; Au, Hg, As, and Sb analyzed by INAA by Activiation Laboratories, Ancaster, Ontario; total sulfur analyzed by combustion at high temperature followed by infrared detection (LECO); -- = below detection.

of Clark Mineralized Samples

anhydrite–rich						Silica	Fe-Mn-Silica			Silica-clay			Barite-silica-clay			
Clark-3A	Clark-3C	P5-623-11R	P5-634-8R	P5-634-10R	P5-623-8R	P5-623-17A	P5-623-3SS	P5-623-18min	SO135-74DR3	SO135-74DR6	SO135-74DR7	SO135-74DR11	Clark-1	SO135-74DR1	SO135-74DR4	SO135-74DR5
0.15	7.25	0.61	1.19	0.06	3.33	0.14	3.35	4.35	4.33	1.08	0.02	3.85	46.8	29.8	37.8	26.2
33.2	34.1	38.5	39.8	39.06	37.04	0.12	1.33	1.21	2.59	0.23	8.97	0.28	0.16	0.21	0.17	0.38
0.5	<0.5	0.16	0.08	0.19	0.14	87.91	27.6	27.18	18.3	68.2	52.9	63.3	10.0	30.6	17.4	43.2
5.72	0.17	1	0.42	2.34	0.8	3.33	38.2	28.78	2.02	3.15	9.29	1.47	0.41	0.54	1.29	1.42
<0.02	<0.02	<0.001	<0.001	<0.001	<0.001	0.003	0.082	0.021	0.24	0.48	0.74	0.53	0.03	0.17	0.08	0.19
0.2	<0.2	0.03	0.02	0.07	0.04	0.06	1.7	0.51	6.6	13.2	19.4	13.6	0.8	4.5	2.4	4.7
<0.01	<0.01	0.007	<0.001	<0.001	0.002	0.227	1.594	20.48	25.5	0.01	0.14	<0.01	0.13	0.5	0.45	<0.01
0.11	0.04	0.04	0.05	<0.01	0.04	0.17	1.23	1.34	1.54	1.32	3.88	1.63	0.15	0.69	0.38	0.59
0.37	0.19	0.39	0.28	0.03	0.34	0.79	4.8	3.17	2.01	0.76	2.75	1.01	0.2	0.46	0.18	0.42
0.06	0.05	<0.01	<0.01	0.01	<0.01	0.17	0.82	0.87	0.55	2.05	0.3	0.69	0.06	0.12	0.29	0.32
0.2	0.1	0.29	0.44	0.26	0.33	0.29	1.36	0.92	0.2	0.2	0.1	0.1	0.1	0.1	0.1	0.2
0.01	0.02	<0.01	<0.01	<0.01	<0.01	0.05	0.98	0.63	0.1	0.02	0.08	0.03	0.01	0.01	0.02	0.01
24.7	21.8	24.4	26	25.8	25	0.09	0.98	1.04	3.46	1.97	<0.02	1.28	12.2	7.84	11.3	6.92
8.9	1.5	9.2	1.9	9.9	6.4	6.9	20.8	15.4	10.5	7.2	2.6	8.4	1.2	3.7	1.9	3.4
1,170	2,160	3,221	2,367	1,735	3,339	216	1,137	1,865	3,170	191	217	1,370	9,550	6,190	5,900	3,920
1.2	0.19	<2	<2	4	<2	3	9	9	7.4	45	5.3	14	1.4	4	8.4	8.5
0.05	0.03	<0.5	<0.5	<0.5	<0.5	<0.5	<0.5	1.2	0.74	8.9	1.6	3.7	0.23	2.2	0.94	1.7
<0.5	<0.5	<1	<1	<1	<1	<1	<1	<1	<0.5	<0.5	<0.5	<0.5	<0.5	<0.5	<0.5	<0.5
18.9	--	13.6	14.3	0.8	12.6	35.4	179	102	5.6	<0.5	5.3	<0.5	6.8	5.8	<0.5	3.4
<5	<10	<5	<5	<5	<5	<5	<5	<5	<10	71	30	20	<5	28	25	26
6	<5	<5	<5	<5	<5	<5	66	105	112	228	277	224	16	85	35	87
0.5	<0.5	<0.1	<0.1	0.1	<0.1	0.2	3.6	0.7	13	30	31	23	1.4	9.3	2.9	10
0.5	0.12	<0.1	<0.1	0.2	<0.1	0.4	0.9	3.8	1.9	15	0.24	2.1	0.74	1.4	2.6	2.3
0.03	0.05	<0.1	<0.1	<0.1	<0.1	<0.1	<0.1	0.3	0.11	0.17	0.32	0.23	0.04	0.06	<0.02	0.1
0.22	<0.05	<1	<1	<1	<1	<1	<1	<1	0.23	0.37	0.61	0.43	0.07	0.12	<0.05	0.16
2.6	<0.5	12	7	16	<4	129	13	<4	32	211	132	50	2.6	37	28	35
2.6	0.69	<2	<2	<2	<2	<2	8	5	9.7	13	19	14	0.72	2.6	1.9	3.7
0.07	<0.05	0.3	<0.2	0.4	0.4	2.7	0.3	0.3	0.73	4.4	3.1	1.3	0.08	0.79	0.59	0.76
0.23	<0.05	<0.1	<0.1	<0.1	0.3	0.1	<0.1	<0.1	<0.05	<0.05	<0.05	0.06	0.11	<0.05	<0.05	<0.05
34	--	<1	<1	9	6	4	2	3	82	<1	<1	<1	22	<1	<1	<1
504	--	34.5	22.6	152	30.9	99.7	724	631	57.1	80.2	<0.5	26.5	20.2	6.6	45.6	40.2
10.9	3	7.5	3.1	2.3	6.9	6	5.4	20.2	20	4.8	0.3	6.7	13.2	7.2	2.6	1.6
7	--	29	16	<1	31	41	<1	66	5	48	<1	28	140	130	<1	66
790	13	148	103	974	137	8	11	14	162	393	127	43	45	17	74	40
94	54	303	117	234	300	24	24	110	128	3,860	114	53	300	82	107	82
540	12	242	102	310	401	12	14	24	64	1,240	4	58	240	71	278	69
39	11	17.1	8.9	11.2	21	0.4	1.4	<0.3	1.3	13	0.2	1.5	16	21	3.4	7.5
2,250	--	1,530	682	896	1,430	<2	43	<2	20	8,110	22	55	225	137	455	275
<0.2	<0.2	<0.4	<0.4	<0.4	<0.4	<0.4	<0.4	<0.4	<0.2	<0.2	<0.2	<0.2	<0.2	<0.2	<0.2	<0.2
0.6	0.2	5	1.7	2	5.1	7.4	<0.5	5.1	1	8.3	<0.2	<0.2	<0.2	<0.2	0.3	0.6
0.7	0.2	<1	<1	<1	<1	3	3	14	18	20	17	11	2.7	6.2	4.9	4.6
		<1	<1	<1	<1	5	14	31								
2.8	2.4	<0.1	<0.1	<0.1	<0.1	0.3	0.1	<0.1	4.5	0.44	0.06	0.72	2.7	0.73	0.57	2.5
<0.05	<0.05	<0.2	<0.2	<0.2	<0.2	<0.2	<0.2	<0.2	<0.05	<0.05	0.05	<0.05	<0.05	0.07	<0.05	0.08
<0.5	<0.5	<1	<1	<1	<1	<1	<1	<1	<0.5	0.6	<0.5	0.6	1	<0.5	1.7	1.7
17	<5	<1	<1	<1	<1	2	3	17	599	21	25	<5	7	7	7	<5
<3	--	<3	<3	<3	<3	<3	<3	<3	<3	4	<3	<3	<3	<3	<3	<3
<0.2	<0.2	--	--	--	--	--	--	--	0.5	0.9	<0.2	0.4	<0.2	<0.2	0.3	0.3
0.7	0.3	<2	<2	6	<2	13	78	798	490	6.7	0.8	0.8	2.9	8.6	11	1
16	<10	<1	<1	1	<1	<1	2	30	93	15	11	<10	<10	<10	<10	<10
2.2	0.2	0.8	0.9	0.6	0.8	<0.1	0.8	1.6					1.2			
4.9	0.8	1.2	1.5	1.2	1.2	0.1	1.2	1.9					1.3			
0.75	0.2	0.16	0.17	0.16	0.14	<0.05	0.19	0.28					0.13			
3.8	1.8	0.7	0.8	0.8	0.6	0.1	1.2	1.4					0.5			
0.91	0.28	0.2	0.2	0.3	0.2	<0.1	0.5	0.4					0.07			
0.3	0.15	1.47	0.38	0.23	0.72	<0.05	0.72	0.4					<0.02			
0.87	0.27	0.2	0.2	0.3	0.2	<0.1	1	0.8					0.07			
0.11	0.05	<0.1	<0.1	<0.1	<0.1	<0.1	0.2	0.1					<0.02			
0.47	0.14	0.1	0.2	0.2	0.1	0.2	1.3	0.9					0.08			
0.08	0.04	<0.1	<0.1	<0.1	<0.1	<0.1	0.3	0.2					0.02			
0.16	0.05	<0.1	<0.1	<0.1	<0.1	0.1	0.8	0.6					0.06			
0.02	0.02	<0.05	<0.05	<0.05	<0.05	<0.05	0.12	0.09					<0.02			
0.1	0.04	<0.1	<0.1	<0.1	<0.1	0.1	0.7	0.6					0.08			
<0.02	0.03	<0.04	<0.04	<0.04	<0.04	<0.04	0.1	0.09					<0.02			

Clark-4A, -4B, etc., are subsamples related to the "fisherman" mineralized sample (74DR-12 in Tables 2 and 3) recovered by local fishermen in their nets immediately before the *Sonne* 135 cruise

APPENDIX 2B. REE Data for Clark Mineralized Samples Plotted in Figure 11

	P5-623-11R white	P5-623-11R gray	P5-623-11R yellow	P5-623-8R white	P5-623-8R gray	SO135-74DR 12-2	SO135-74DR 12-3	SO135-74DR 12-4
La (ppm)	0.516	0.342	0.227	0.354	0.886	0.489	0.202	0.472
Ce	1.033	0.713	0.399	0.783	1.873	0.549	0.259	0.508
Pr	0.147	0.103	0.041	0.120	0.275	0.044	0.024	0.039
Nd	0.641	0.478	0.121	0.572	1.298	0.128	0.068	0.101
Sm	0.153	0.115	0.018	0.142	0.315	0.016	0.009	0.008
Eu	0.444	0.312	0.059	0.218	0.754	0.024	0.010	0.015
Gd	0.182	0.139	0.021	0.173	0.375	0.018	0.012	0.010
Tb	0.024	0.019	0.002	0.022	0.051	0.002	0.002	0.001
Dy	0.127	0.097	0.011	0.108	0.273	0.009	0.007	0.004
Ho	0.020	0.017	0.002	0.018	0.044	0.001	0.001	0.001
Er	0.048	0.037	0.004	0.037	0.098	0.004	0.003	0.002
Tm	0.005	0.004	0.000	0.003	0.009	0.000	0.000	
Yb	0.022	0.015	0.003	0.014	0.045	0.002	0.003	
Lu	0.002	0.002	0.001	0.001	0.005	0.000	0.000	

APPENDIX 3. Mixtures of New Barite and Reworked Old Barite

Theoretical mixtures: New barite plus ^{226}Ra and ^{228}Ra
Old barite plus decayed ^{226}Ra only

% new barite	$^{228}Ra/Ba$ Bq·g^{-1}	$^{226}Ra/Ba$ Bq·g^{-1}	$^{228}Ra/^{226}Ra$ Bq·Bq^{-1}
100	90	30	3.00
90	81	29	2.79
60	54	26	2.08
40	36	24	1.50
10	9	21	0.43
0	0	20	0.00

Theoretical mixing line for new and old barite

$y = 0.1111x + 20$

The proportion of old to new barite determines the $^{228}Ra/^{226}Ra$ value at the time of mineralization. The intercept gives the $^{226}Ra/Ba$ value for old barite and hence its age can be calculated

Clark volcano

Sample PV No.	% new barite	$^{228}Ra/Ba^1$ Bq·g^{-1}	$^{226}Ra/Ba$ Bq·g^{-1}	$^{228}Ra/^{226}Ra$ Bq·Bq^{-1}
623-4 min	68.5	12.24 ± 0.15	16.41 ± 0.17	0.75 ± 0.01
623-5SS	46.3	8.27 ± 0.42	11.38 ± 0.13	0.73 ± 0.04
623-6B-1a	11.3	2.01 ± 0.09	7.22 ± 0.08	0.28 ± 0.01
623-7R	55.3	9.88 ± 0.17	11.66 ± 0.12	0.85 ± 0.02
623-8R	100.0	17.70 ± 0.50	18.68 ± 0.29	0.95 ± 0.03
623-11R	90.4	15.99 ± 0.45	17.14 ± 0.25	0.93 ± 0.03
634-3R	47.6	8.50 ± 0.14	11.25 ± 0.13	0.76 ± 0.02
634-8R	100.0	18.19 ± 0.38	19.65 ± 0.25	0.93 ± 0.02
634-9-RB-1	44.0	7.85 ± 0.15	13.45 ± 0.15	0.58 ± 0.01
634-9-RB-2	51.8	9.24 ± 0.18	14.11 ± 0.15	0.65 ± 0.01
		Average and stdev		0.74 ± 0.20

Chimneys and crust Clark volcano

$y = 0.73x + 6.05$
$R^2 = 0.92$

From the intercept, the age of old barite = 2720 ± 330 yrs

Brothers volcano (Lena chimney)

Sample	% new barite	$^{228}Ra/Ba^1$ Bq·g^{-1}	$^{226}Ra/Ba$ Bq·g^{-1}	$^{228}Ra/^{226}Ra$ Bq·Bq^{-1}
851-3A-1	91.0	53.6 ± 1.5	21.6 ± 0.3	2.48 ± 0.08
851-3A-2	91.6	54.9 ± 1.5	21.7 ± 0.3	2.53 ± 0.08
851-3A-3	100.0	59.9 ± 0.5	23.7 ± 0.2	2.52 ± 0.03
851-3A-4	86.4	52.0 ± 1.3	20.5 ± 0.3	2.54 ± 0.07
851-3A-5	98.8	59.3 ± 0.7	23.4 ± 0.2	2.53 ± 0.04
851-3A-6	96.7	55.2 ± 1.2	22.9 ± 0.3	2.40 ± 0.06
851-3A-7	98.7	59.0 ± 1.0	23.4 ± 0.3	2.52 ± 0.05
851-3A-8	91.9	55.0 ± 0.6	21.8 ± 0.2	2.52 ± 0.04
851-3A-9	86.8	51.4 ± 0.5	20.6 ± 0.2	2.49 ± 0.03
	93.5	Average and stdev		2.50 ± 0.04

'Lena' chimney Brothers volcano

$y = 0.37x + 1.47$
$R^2 = 0.91$

^{1} $^{228}Ra/Ba$ values are adjusted to the time of mineralization